Optogenetic manipulation of individual or whole population *Caenorhabditis elegans* worms with an under hundred-dollar tool: the OptoArm.

M. Koopman[1*], L. Janssen[1], E.A.A. Nollen[1*]

[1]European Research Institute for the Biology of Ageing, University of Groningen, University Medical Centre Groningen, The Netherlands

*Corresponding authors: m.koopman@umcg.nl or e.a.a.nollen@umcg.nl

Abstract

Optogenetic tools have revolutionized the study of neuronal circuits in *Caenorhabditis elegans.* The expression of light-sensitive ion channels or pumps under specific promotors allows researchers to modify the behavior of excitable cells. Several optogenetic systems have been developed to spatially and temporally photoactivate light-sensitive actuators in *C. elegans*. Nevertheless, their high costs and low flexibility have limited wide access to optogenetics. Here, we developed an inexpensive, easy-to-build, and adjustable optogenetics device for use on different microscopes and worm trackers, called the OptoArm. The OptoArm allows for single- and multiple-worm illumination and is adaptable in terms of light intensity, lighting profiles and light-color. We demonstrate the OptoArm's power in a population-based study on contributions of motor circuit cells to age-related motility decline. We find that functional decline of cholinergic neurons mirrors motor decline, while GABAergic neurons and muscle cells are relatively age-resilient, suggesting that rate-limiting cells exist and determine neuronal circuit aging.

Keywords: OptoArm, Optogenetics, *Caenorhabditis elegans,* neuronal ageing, rhodopsin, worm-trackers.

Introduction

Neurotransmission is defined as the process by which neurons transfer information via chemical signals at synaptic contacts (e.g. synapses) with target cells. Those target cells can be other neurons, but also non-neuronal cell types (e.g. muscle cells). *Caenorhabditis elegans* has proven to be an important model organism to study fundamental neurobiology, including neurotransmission at chemical synapses (Rand et al., 1984; 1985; Lewis et al., 1987;

30 Hosono et al., 1989; 1991; Maruyama et al., 1991; Nonet et al., 1993, 1998; Jorgensen et al., 1995; Miller et al.,
31 1996; Goodman et al., 1998, 2012; Richmond et al., 1999a, 1999b, 2006, 2009; Francis et al., 2003; 2006). As a
32 matter of fact, important molecular players involved in synaptic transmission, synaptic vesicle docking, priming,
33 fusion and recycling have actually been discovered in *C. elegans* and are highly conserved in mammalian systems
34 (Brose et al., 1995; Betz et al., 1998; Aravamudan et al., 1999; Augustin et al., 1999; Richmond et al., 1999b;
35 Lackner et al., 1999; Sassa et al., 1999). Initially, pharmacological assays were predominantly used to analyze
36 synaptic transmission and its associated molecular substrates in *C. elegans* and to determine whether an observed
37 neurotransmission defect was pre- or postsynaptic of nature (Lewis et al., 1987; Miller et al., 1996). Then, the
38 development of electrophysiology resulted in new techniques that have allowed researchers to study the electrical
39 events that occur at synapses more directly (Richmond et al., 1999a, 1999b, 2006, 2009; Francis et al., 2003; 2006;
40 Mellem et al., 2002; O'Hagan et al, 2005; Ramot et al., 2008a; Kang et al., 2010; Geffeney et al., 2011; Kawano
41 et al., 2011; Goodman et al., 2012). These methods provide a quantifiable readout for the underlying synaptic
42 activity and a way to investigate synaptic properties. Nevertheless, standard electrophysiology in *C. elegans* is
43 technically challenging and cannot be performed in intact worms, making it impossible to directly correlate
44 synaptic activity with behavioral readouts (Husson et al., 2013). The development of optogenetics, however,
45 addressed this issue and created the possibility to directly manipulate synaptic activity and simultaneously look at
46 behavioral changes (Nagel et al., 2005; Liewald et al., 2008; Liu et al., 2009; Schultheis et al., 2011a; 2011b;
47 Husson et al., 2013).
48 Optogenetics is based on the genetic expression of a light-sensitive actuator that can actively influence
49 biochemical reactions or neuronal activity in response to a non-invasive light stimulus (Zhang et al., 2007; Husson
50 et al., 2013). The most common used 'actuators' are the rhodopsins, which have been discovered in algae, and are
51 now widely used in different cells and organisms to depolarize or hyperpolarize cells upon light stimulation (Nagel
52 et al., 2003, 2005, Li et al., 2005; Schroll et al., 2006; Bi et al., 2006; Ishizuka et al., 2006; Zhang et al., 2007;
53 Fang-Yen et al., 2015). The transparent body of *C. elegans*, its amenability for genetic manipulation and its
54 invariant nervous system, make the worm ideal for optogenetic manipulation (Hope et al., 1999; Kaletta et al.,
55 2006; Antoscheckin et al., 2007; Husson et al., 2013). In fact, *C. elegans* was the first multicellular organisms to
56 have its behavior manipulated *in vivo* by the photoactivation of channelrhodopsin-2 (ChR2) in muscle cells (Nagel
57 et al., 2005). ChR2 is a light-sensitive cation channel that can undergo a light-induced conformational change,
58 thereby allowing H^+, Na^+, K^+ and Ca^{2+} ions to passively diffuse down their concentration gradients (Figure 1A)
59 (Nagel et al., 2003, 2005; Kolbe et al., 2000). In excitable cells, this results into rapid depolarization of the plasma

membrane and the subsequent initiation of downstream events, like fibril contraction in muscle cells and synaptic vesicle release in neuronal cells (Nagel et al., 2005; Zhang et al., 2007; Liewald et al., 2008; Almedom et al., 2009; Liu et al., 2009; Gao et al., 2011; Schultheis et al., 2011b; Kittelman et al., 2013). The specificity of the response is acquired by expressing optogenetic proteins under specific promoters (Figure 1B) in the worm. For instance, the expression of ChR2 in motor neurons (*unc-47, unc-17*) or muscles (*myo-3*) elicits either a flaccid or spastic paralysis upon complete illumination of the worms (Zhang et al., 2007; Liewald et al., 2008; Husson et al., 2013). This obvious and robust response results in a change in body length that can be used as a clear readout (Figure 1C) (Zhang et al., 2007; Liewald et al., 2008). Multiple other strains exist, in which for example specific interneurons or sensory neurons are under the control of ChR2 (Nagel et al., 2005; Franks et al., 2009; Guo et al., 2009; Narayan et al., 2011; Lindsay et al., 2011; Milward et al., 2011; Piggott et al., 2011; Leifer et al., 2011; Stirman et al., 2011; Faumont et al., 2011; Husson et al., 2012a; Busch et al., 2012; Schmitt et al., 2012). Functional ChR2 requires the chromophore all-trans retinal (ATR), which is not endogenously produced by *C. elegans*. Exogenous feeding of ATR can circumvent this problem and ensures functional ChR2 (Nagel et al., 2005)

Over the years, multiple systems have been developed to illuminate *C. elegans* in a temporal and/or spatial manner for optogenetic experiments. Most of those systems are custom built and include fluorescence microscopes, or systems with lasers and shutters (Leifer et al., 2011; Weissenberger et al., 2011; Stirman et al., 2010; 2011; Husson et al., 2012b; Qiu et al., 2015; Rabinowitch et al., 2016a; Gengyo-Ando et al., 2017). These systems require costly equipment and are mostly designed for single-animal illumination. While the costs might limit the general use of these systems for a general audience, they do, however, provide clear benefits for fundamental research requiring single-cell stimulation. For example, some of these systems provide ways of following single worms in space and time with chromatic precision, thereby ensuring exact illumination of a specified anatomical position (Stirman et al., 2011; Leifer et al., 2011; Kocabas et al., 2012; Gengyo-Ando et al., 2017). This targeted illumination makes it possible to optogenetically excite single neurons for which specific promotors are not known (Kocabas et al., 2012). Moreover, in these expensive systems, one can adjust the light intensity relatively easily, making the systems flexible and adaptable for different types (e.g., short- or long-term) of experiments.

Several researchers have tried to make optogenetical experiments more accessible to a wide audience by successfully developing inexpensive (<1500 dollars) optogenetic systems (Pulver et al., 2011; Kawazoe et al., 2013; Rabinowitch et al., 2016b; Pokala et al., 2018; Crawford et al., 2020). Some of these low-cost systems even allow multiple worms to be illuminated at the same time (Kawazoe et al., 2013; Crawford et al., 2020). When

90 considering the current developments of automated worm trackers (Tsibidis et al., 2007; Ramot et al., 2008b;
91 Swierczek et al., 2011; Stirman et al., 2011; Leifer et al., 2011; Wang et al., 2013; Kwon et al., 2013; Restif et al.,
92 2014; Javer et al., 2018; Perni et al., 2018; Koopman et al., 2020), the ability to illuminate multiple worms at the
93 same time during tracking offers a clear benefit for studying both population and single-worm characteristics.
94 However, there are also clear limitations of these low-cost systems. In fact, most of the systems require manual
95 adaptations (e.g., aluminum foil, closed boxes) to ensure a light intensity that is high enough (e.g. 1.6 mW/mm^2,
96 or at least 1.0 mW/mm^2) for optogenetic purposes in *C. elegans* (Rabinowitch et al., 2016b; Crawford et al., 2020).
97 These adaptations make the simultaneous tracking of illuminated worms challenging and highly reduce the
98 adaptability of the system to other experimental set-ups. Moreover, within low-cost systems the light-source often
99 has to be placed in very close proximity (<2 cm) to the worms, which makes such systems not suitable for long-
100 term stimulation due to potential heat generation and phototoxicity (Kawazoe et al., 2013; Rabinowitch et al.,
101 2016b; Crawford et al., 2019). Some systems, such as the OptoGenBox (Busack et al., 2020), are exempt from
102 these issues, but they are also more expensive.

103 Clearly, there is no shortage of tools and techniques to perform optogenetic experiments with *C. elegans*.
104 Ideally, one would simply look at all the advantages and limitations of each system and select for the platform that
105 fits best to the biological questions to be answered. Practically, however, there are often different types of
106 biological questions to be answered or various approaches required to tackle a specific hypothesis. We argue that
107 the use of optogenetics should not be restricted by limited capabilities of single system or available (financial)
108 resources. From that perspective there remains a challenge in developing low-cost optogenetic devises with high
109 flexibility and adaptability. Here, we describe in detail how we developed an under hundred-dollar optogenetic
110 device, the OptoArm. This system provides the user with an easy-to-build, highly adaptable, flexible and reliable
111 optogenetic system. The arm allows integration in different experimental set-ups and tackles both single- and
112 multiple-worm illumination, making combinatory approaches and population-based studies possible. In fact, we
113 demonstrate the use of the OptoArm by determining the functional contribution of motor circuit cells to the age-
114 related decline in motility. Finally, by offering both the option to build a manual and a fully automated system,
115 researchers are able to pick the set-up that fits their budget and requirements best. The biologically and technically
116 validated OptoArm makes optogenetics experiments accessible for researchers both within and outside the
117 laboratory, including teaching institutions.
118

119 # Results

120 **Efficient thermal management is key in constructing a compact, inexpensive set-up**

121 *Construction.* To build a simple and inexpensive optogenetics device that can be adjusted to laboratory-specific
122 parameters, specific applications and requirements, we investigated the use of low-cost, high-intensity LEDs with
123 interchangeable optics. The ease of the construction and the low costs of the system ensures accessibility for both
124 researchers and students. We opted for a straightforward electronic circuitry (Figure 2A) using a 700 mA LED-
125 driver to ensure the feeding of fixed electric current to a 1.03 W LED with a wavelength ranging between 440-460
126 nm (optimal: 448 nm). The placement of the ON/OFF switch between the CTRL and REF pins, in parallel with
127 the potentiometer (Figure 2A, main panel), provides the best management of inrush power and spikes to the LED.
128 Therefore, this is the recommended configuration to ensure an optimal lifetime for the LED. For prototyping
129 purposes, however, we used a circuit with the switch serially connected to the LED driver and the DC plug (Figure
130 2A, insert). As depicted in Figure 2B, in addition to the high-intensity LED and the LED-driver, only a small set
131 of components is required (see Table 1 and *Material and methods*): a potentiometer to adjust intensity, an ON/OFF
132 switch, a lens holder (home-made) with interchangeable lenses, a heatsink and thermal adhesives to connect the
133 components (see *thermal stability* section) and a $9V_{DC}$ adapter to power the system. The different steps required
134 to build the optogenetic arm can be found in Figure 2C and Table 2. Eventually, we installed the complete circuitry
135 on a standard flask clip clamp, as this could be used in combination with different stands for different set-ups
136 (figure 2D, E, Table 1). Note that the combination of the wavelength and high intensity makes the LED dangerous
137 for the human eye. Try to avoid looking directly into the LED, use protective sheets or wear protective glasses.

138 The resulting OptoArm is compact in nature, making it easy to move around and integrate within different
139 recording systems. The prices in Table 1 are an approximation based on the main components. They do not include
140 the required, basic soldering materials, extra wires, shrink tubing and pin-adaptors, nor standard *C. elegans*
141 equipment, like a microscope. We were able to reduce our costs further (<65 dollar) by recycling available material
142 in the lab, including the flask clip clamp and different stands. Therefore, it should be underlined that almost all
143 components of the OptoArm can be substituted for cheaper alternatives that may be readily available. The
144 mounting and optical components (Table 1) can be easily interchanged with alternatives. The required components
145 related to thermal management, however, are highly dependent on the requirements of the electronical components
146 (see *thermal stability* section). Moreover, the choice for the specific LED-driver in this paper is also related to the
147 possible automation of the system, which we will touch upon in later sections. In the end it comes down to the

user to verify that any alternative components meet the required specifications of the system and that the system still performs adequately for the desired experimental set-up.

Thermal management. Although LEDs rank among the most efficient sources of illumination a large portion of the input power is still converted to heat (Lin et al., 2011; Fang et al., 2017). It is important to have adequate thermal management to remove this waste heat by either conduction or convection, as excessive increases in temperature at the LED junction directly affect LED-performance. In a short-term this could result in color shifts and reduced light output (intensity), while in the long-term accelerated lumen depreciation may take place (Park et al., 2005; Lee et al., 2011; Huang et al., 2015; Han et al., 2015; Dalapati et al., 2016). While the so-called "T-droop", i.e. the efficiency droop with increasing temperature, is more pronounced in AlGalnP-based LEDs (e.g., red LEDs); blue InGaN-LEDs still suffer from (minimal) color shifts and decreased output due to high junction temperature (Kim, et al., 2016; Fu et al., 2018; Oh et al., 2019). The junction temperature of an LED is determined by three parameters: drive current, heat dissipation and the ambient temperature (Kim et al., 2016). While the drive current can be kept stable with fixed-current drivers and ambient temperature can be controlled for in climate-controlled rooms, efficient heat removal generally requires extra management. Heat is typically transferred away and dissipated from the LED using passive systems like heat sinks (Figure 2F). The required thermal properties of such a heat sink can be calculated by using a basic thermal model: see box 1. We selected a 5.2 ºC/W heatsink that fulfills our criteria for a system with appropriate thermal cooling. It is important to underline that the measured junction temperature is higher than theoretically expected when using a heatsink of 5.2 ºC/W (see box 1). Therefore, it is critical to use a safe margin when selecting a heatsink and to verify the actual junction temperature instead of simply relying on the thermal equation.

Lighting area and intensity is stable and can be adjusted to experimental requirements through exchangeable lenses and adjustable working distance.

Next, we explored the usability of the OptoArm for experimental purposes with *C. elegans*. We evaluated different aspects of the system that are critical for optogenetics, starting with light intensity and stability. The Royal blue Luxeon Rebel LED of the OptoArm has a beam angle of 125º, which results in a large surface being illuminated. As intensity is the function of power divided by surface, there are simply two parameters that determines the intensity of a system: 1) area being illuminated, 2) the power of the LED. The maximal power of the LED (1.03 W) at a current of 700 mA is fixed and cannot be further enhanced. However, the area that is illuminated can be reduced by either decreasing the working-distance (WD) or applying convex optics to concentrate the light beam

178 to a smaller surface. Since optogenetic experiments in *C. elegans* require an intensity of at least 1.0 mW/mm^2 and
179 preferably 1.6 mW/mm^2 (Nagel et al., 2005; Liewald et al., 2008; Schmitt et al., 2012; Husson et al., 2013), we
180 explored the produced intensity of the OptoArm without and with several low-cost lenses (Figure 3A, B).

181 To compare the different set-ups, we used a fixed working-distance of 5 cm between the LED and the
182 surface to be illuminated. With a power meter set to 448 nm, we measured the light intensity of 29 different *x,y*
183 coordinates in an area of 4 by 4 cm using a 'hot-spot' approach (Figure 3C). From those collected measurements
184 we generated integrated intensity profiles (Figure 3D). We observed clear differences in the acquired intensity
185 profiles between the different set-ups. Without a lens, the illumination is relatively uniform, while using lenses
186 that narrow the angle of the light beam result in more pronounced gaussian-like profiles with clear intensity peaks
187 in the middle. The combination of the OptoArm with a 10º lens fulfills the required intensity of 1.6mW/mm^2. In
188 order to assess the stability of these profiles, we collected 1000 (~ 1 minute) readings per set-up at the *x,y*
189 coordinate with the highest intensity, thereby assuming an gaussian-distributed light source. For all the set-ups,
190 the readings were steady and consistent, as evidenced by the narrow distributions (Figure 3D, 3E). Clearly, adding
191 different convex lenses to the OptoArm can modify the output of the system in terms of measured light-intensity
192 (Figure 3E). Note that the readings in the histograms (Figure 3D, E) are lower than those seen in the intensity
193 profiles (Figure 3D). The latter can be explained by the different measuring methods (software-related) that were
194 used: hot-spot detection versus a gaussian assumption.

195 Although most optogenetic experiments only take a few milliseconds, or a minute at its maximum
196 (Busack et al., 2020), we also assessed the stability of the system in terms of intensity over several minutes (Figure
197 3F). With the same working-distance of 5 cm, we assessed the maximum intensity at 0, 5, 10 and 20 minutes after
198 turning the LED on. Again, we collected 1000 readings per timepoint. The ON-time of the LED had no influence
199 on the measured intensity without a lens (Figure 3G), while only a minor drift in intensity (<0.02 mW/mm^2 in 20
200 minutes) was observed with the 10º lens (Figure 3H). Therefore, we conclude that the OptoArm, in its current set-
201 up, performs well in terms of intensity and stable output over time.

202

203 **Due to its compact and highly flexible nature, the OptoArm is compatible with both single- and**
204 **multi-worm imaging platforms**

205 When using the OptoArm with a microscope or any tracking platform (e.g. the WF-NTP), the angle of incidence
206 of the blue light is in most cases not perpendicular to the surface as a consequence of practical limitations, e.g. the
207 arm should not block the light-pad from the sample to the ocular or camera (Figure 4A). The consequence of

208 working under a non-perpendicular angle is that intensity profiles will deform due to increases and decreases of
209 the path length of specific parts of the light beam (Figure 4B, C). The intensity of light as a function of the distance
210 from the light source follows an inverse square relationship. Therefore, increased path lengths will result in a
211 significant reduction of the light intensity.

212 To validate the OptoArm in an actual experimental set-up, we again generated integrated intensity profiles
213 and stability measurements of the three lenses when used with a standard dissection microscope (Figure 4). As
214 expected, both the hot-spot intensity and the steady-state measurements pointed out that the maximal intensity is
215 decreased when working under a non-perpendicular incidence angle (Figure 4D). However, the acquired intensity
216 with a 10º lens still reaches the required 1.6mW/mm^2 (WD: ~3.5 cm) and with some fine-adjustments in height
217 (i.e. working distance) and angle, the intensity even exceeds this number (see also Figure 5). More importantly,
218 the area with the required intensity (1.6mW/mm^2) is large enough to ensure the whole visible microscopic surface
219 being illuminated with the same intensity (see Figure 4E for details). In fact, an area with a ~ϕ 1 cm appears to
220 fulfil the required 1.6 mW/mm2 (Figure 4D) and this area corresponds with the visible microscopic surface at a
221 total magnification of 30 x (Figure 4E, 2.0x).

222 Having established and validated a microscope set-up, we moved on to an experimental set-up involving
223 a multi-worm tracker (Figure 4F). When working with a platform that allows multiple worms to be tracked at the
224 same time, it is critical that illumination and light intensity are as uniform as possible at all *x,y* coordinates in the
225 region of interest (ROI). Spatial consistency is relevant in order to reduce individual variation. Clearly, lenses that
226 generate narrower gaussian-like profiles (Figure 4D) do not meet those criteria, even though they do provide the
227 adequate intensity. Consequently, we only generated intensity profiles of the OptoArm with the 21º lens at two
228 different working-distances (Figure 4G) and a fixed incidence-angle of 43º. While far from perfect, the 21º lens is
229 offers the best compromise between uniform illumination and high intensity (0.75-1.0 mW/mm^2) when using 3-
230 cm worm plates (Figure 4G). Moreover, systems like the WF-NTP make it possible to only analyze worms in a
231 specific ROI, which would make it possible to account for spatial inconsistency of illumination at the edges of a
232 plate. If the experimental conditions allow it, one can also simply use smaller plates, e.g., 12-wells, to better fit the
233 intensity profiles. Finally, it should be underlined that the adaptability of the OptoArm makes it easy to further
234 enhance the system e.g. by using triple-LED systems instead of single LEDs to triple the power of the system
235 (Table 1) if required.

236 Finally, we assessed the intensity of backlights of a standard microscope (maximal intensity) and the WF-
237 NTP (Figure 4H). While, the intensity of those lights is relatively low, it might be sufficient to induce optogenetic

238 responses (Schultheis et al, 2011a). We have tested this hypothesis by comparing the thrashing capacity (i.e. the
239 frequency of lateral bends in liquid) and body length of worms grown with or without ATR with the WF-NTP.
240 Since ATR is required for functional ChR2, non-ATR worms will not respond to blue light and can be used as
241 negative controls (Nagel et al., 2005). We did not find clear evidence for a light-induced response when performing
242 optogenetic experiments with the WF-NTP backlight. Worms grown with or without ATR had a similar thrashing
243 capacity and body length (Figure 4I, J). However, we would recommend to substitute the WF-NTP backlight with
244 a red-shifted variant of 625 nm (Edmund Optics, Red advanced illumination side-fired backlight, #88-411) or to
245 filter out the blue light specifically. This is advisable because several neuronal mutants have been shown to have
246 an increased sensitivity to low-light conditions (Liewald et al., 2008). For microscopic set-ups we suggest to turn
247 down the backlight as much as possible, without compromising the contrast between the worm and its background
248 (Figure 4H).
249

250 **Adjustable intensity levels enable titration of the biological response**

251 All *C. elegans* neurons that have previously been analyzed by photo-electrophysiology exhibited graded
252 transmission. Herein, the release of neurotransmitters directly correlates with the extent of depolarization evoked
253 by light-induced ChR2 activation (Husson et al., 2013). This type of transmission has clear consequences for
254 optogenetic experiments, as changing the light intensity will likely also change transmitter release. Therefore, to
255 properly compare different interventions or different mutants with each other, light intensity should always be
256 consistent and stable throughout complete experiments. On the other hand, the graded transmission in *C. elegans*
257 also allows the 'titration' of the extent of ChR2-induced depolarization by adjustment of the light intensity. In this
258 way, one can modify transmitter release and subsequently also fine-tune the behavioral output (Liewald et al.,
259 2008; Husson et al., 2012a).

260 We explored the adjustability of the OptoArm for 'titration' purposes (Figure 5). First, we created a basic
261 microscopic set-up in which a microscope-based smartphone adapter was used to allow movies being made with
262 a smartphone instead of an expensive camera (Figure 5A). This set-up was completed with a standard blue-
263 light/UV-protection shield to avoid saturation of the camera. Secondly, we used the potentiometer of the OptoArm
264 to adjust the intensity of the system to specific values, without changing the WD or angle of incidence (e.g., 0.2;
265 0.4; 0.8; 1.2; 1.6 and 1.8 mW/mm^2) (Figure 5B). Then, we measured both the stability of each specified light
266 intensity and the accompanying body length of worms expressing ChR2 under the *myo-3* promoter before and
267 during illumination (Figure 5C-F). The normalized body length was then calculated by dividing the body length

268 during illumination by the body length before illumination. We were able to adjust the potentiometer in such a
269 way that the *a priori* specified intensities could be acquired relatively well and were consistently stable over 1000
270 readings (Figure 5C, D). Clearly, adjusting the resistance of the potentiometer of the OptoArm can modify the
271 output of the system in terms of measured light-intensity (Figure 5D). The different light-intensities had dose-
272 dependent effects on normalized body length up till 1.6 mW/mm^2 (Figure 5E,F). Taken all together, the OptoArm
273 allows users to change the light intensity and thus to study its effect on behavioral changes.
274

275 **Perimeter and midline measurements are highly correlated and can be used interchangeably as**
276 **a readout for body length.**

277 Before continuing with the biological validation of the OptoArm, we first took the time to explore the possible
278 methods to quantify changes in body length during an optogenetic experiment. In general, to follow changes in
279 body-length over time, one can manually draw a midline through the worm from head to tail before and during
280 blue-light stimulation (Figure 5). Clearly, this labor-intensive scoring method is vulnerable to inconsistency and
281 experimenter bias and becomes impractical when scoring many worms and conditions. There are Matlab codes
282 available to automate and streamline these measurements (Liewald et al., 2008; Crawford et al., 2020), but these
283 codes also require a basic understanding of programming languages and access to Matlab. Based on the idea that
284 the OptoArm should be a simple system that is accessible to the whole community, we aimed to simplify the
285 accompanying analysis for 'Δ body length', i.e. the change in body length upon optogenetic stimulation, as well.
286 Therefore, we explored the use of the opensource software ImageJ to analyze the optogenetic data in a semi-
287 automatic way (Figure 6).

288 It has been stated that the perimeter of the worm is equal to two times the body length plus two times the
289 diameter (Kammenga et al., 2007). Since the perimeter can be easily measured and is more often used as a way to
290 represent body length in *C. elegans* (Fujiwara et al, 2002; Kammenga et al., 2007; Nussbaum-Krammer et al.,
291 2015), we created a sequential pipeline in ImageJ with the perimeter as readout (Figure 6A). All steps of this
292 ImageJ pipeline, and the accompanied methods, are included in the material and method section. In short, the
293 pipeline focusses on enhancing contrast, subtracting background and thresholding to yield a set of binary images
294 from the worm without gaps or ruffled edges. The binary images are used to measure the perimeter of the worm
295 in each frame. Since all steps are performed on complete movies, the end-result is a list of perimeters for a single
296 worm over time. In Figure 6B, the raw perimeter measurements of a worm expressing ChR2 under the *myo-3*
297 promoter, before, during and after optogenetic stimulation are plotted. By normalizing all individual measurements

298 of a single worm to the average perimeter in the first 60 frames (light OFF) one can create kinetic-plots of the
299 change in perimeter that represent multiple worms (Figure 6C). In order to validate this method, we measured the
300 length of the midline and the accompanying perimeter of 70 individual worms (Figure 6D). The midline and
301 perimeter correlate significantly and therefore appear to be both good estimates of body length (Figure 6E).
302

303 **Optogenetic stimulation of cholinergic and GABAergic mutants with the OptoArm accurately**
304 **reproduces the biological response observed with a more expensive system**

305 To validate the OptoArm and accompanying image-processing biologically, we aimed to reproduce previously
306 described and published optogenetic data on neuronal mutants (Figure 7A). It has been showed that mutations in
307 the *unc-47* gene, which represents the vesicular GABA transporter vGAT (McIntire et al., 1997), translate into the
308 lack of body wall relaxation upon optogenetic stimulation of GABAergic neurons, but increased contractions when
309 cholinergic neurons were photo-stimulated (Liewald et al., 2008). At the same time, mutations affecting the
310 cholinergic system, e.g. *unc-26* that represents the phosholipid phosphatase synaptojanin (Figure 7A), often
311 translate into significantly stronger body-wall muscle contractions upon cholinergic stimulation as well. The latter
312 was initially marked as contradictory as electrophysiological data of those mutants showed reduced electrically
313 evoked postsynaptic currents (ePSCs). However, the paradoxical results are most likely a result of compensatory
314 mechanisms in the muscle, underlining the complementary information that behavioral optogenetic experiments
315 can provide (Liewald et al., 2008).

316 Here, we explored two mutants that have been described in the specified paper, namely *unc-47(e307)* and
317 *unc-26(s1710)*. We used a microscopic set-up (Figure 5A) combined with the OptoArm, thereby ensuring a light
318 intensity of 1.6 mW/mm^2 (Figure 7B). Next, D1 adults expressing ChR2 specifically under the *unc-17* promoter
319 (i.e. expression in cholinergic neurons; *zxIs6*), grown on ATR- or ATR+ plates, were exposed to a regime of 3
320 seconds light off – 3 seconds light on – 3 seconds light off while being recorded. Subsequently, the movies were
321 used to determine the body length over time by a perimeter-approach (Figure 7C) or by measuring the length at
322 fixed timepoints before (500 ms before light ON) and during illumination (1000 ms after light turned ON) with a
323 midline-approach (Figure 7D). Similar to the results described by Liewald et al., we found that *unc-47(e307)* and
324 *unc-26(s1710)* mutants showed significantly stronger photo-evoked contractions (Figure 7C), with clear
325 differences in muscle-relaxation kinetics after the photo-stimulation was terminated. In addition, worms raised at
326 -ATR plates, did not respond to blue light with body contractions and served as appropriate negative controls. The
327 change in body length of the *unc-47* (mean $\pm$ SD: 0.83 $\pm$ 0.020), and *unc-26* mutants (0.85 $\pm$ 0.037) and control

328 (0.91 ± 0.02) worms, as a result of photo-stimulation with the OptoArm, are similar to the numbers found by
329 Liewald et al (2008) (WT: ~0.92, *unc-26*: ~0.87, *unc-47*: ~0.86) (Figure 7D). Next, we also explored the effects
330 of GABAergic stimulation in the *unc-47(e307)* and *unc-26(s1710)* mutants, by expressing ChR2 under the *unc-47*
331 promotor (*zxIs3*). The same lightening regime was used and the body length was again determined by a perimeter-
332 approach (Figure 7E) and a midline-approach (Figure 7F). As expected, *unc-47(e307)* mutants (1.01 ± 0.022)
333 lacked a clear relaxation response, while *unc-26(s1710)* worms (1.06 ± 0.020) behaved much more similar to
334 control worms (1.06 ± 0.020), with the exception of a higher initial peak of relaxation (Figure 7E, F). The same
335 observations were described by Liewald et al., (2008) (WT: ~1.04, *unc-26*: ~1.00, *unc-47*: ~1.04).
336 It has been shown that characteristic defects in neurotransmitter recycling can be reflected by aberrations
337 in long-term photo-stimulation experiments with worms expressing ChR2 under the *unc-17* promoter.
338 Synaptojanin (*unc-26*) is required for endocytotic recycling of synaptic vesicles and mutants are defective in
339 synaptic vesicle budding and uncoating during clathrin-mediated endocytosis (Figure 7A) (Harris et al., 2000;
340 Schuske et al., 2003). The inability to recycle vesicles results in early fatigue of neurons that could potentially
341 translate in the inability to sustain contraction of body wall muscles. Indeed, Liewald et al. (2008) described that
342 wild-type worms normally sustain constant contraction throughout long-term illumination (>60 seconds), while
343 the initially exaggerated body contraction of *unc-26(s1710)* mutants returns quickly to unstimulated levels. We
344 validated this biological data with the OptoArm by following individual worms for 52 seconds, in which worms
345 were constantly illuminated from second 1 to 51 (Figure 7G). While control worms and *unc-47(e307)* mutants
346 showed sustained contraction over the complete interval, *unc-26(s1710)* mutants lost their contractibility already
347 after 8 seconds and returned to wild-type levels after 15 seconds. At the end of the illumination period, the *unc-*
348 *26(s1710)* worms returned to their initial non-illuminated length and thus lost their contraction completely (Figure
349 7G). Altogether, we validated the OptoArm by showing that the inexpensive system can reproduce biological
350 findings acquired with a more expensive fluorescence microscope. The use of the OptoArm with ImageJ provides
351 a sensitive platform to study the various functional aspects related to body contraction, elongation and the kinetics
352 of this behavior.
353
354 **Combination of the OptoArm with various set-ups allows the readout of multiple biological**
355 **parameters for a more comprehensive analysis.**
356 Having a technically and biologically validated system, we continued exploring the use of the OptoArm for
357 different applications and set-ups. Since the platform also allows multi-worm illumination (Figure 4), we explored

358 the use of the OptoArm together with a multi-worm tracking platform, in this case the WF-NTP (Perni et al., 2018;
359 Koopman et al., 2020). It has been previously shown that photo-stimulation of worms on solid substrates,
360 expressing ChR2 under the *unc-47* promotor (GABAergic neurons) or under the *unc-17 promotor*, reduces
361 locomotion speed (Liewald et al., 2008; Kittelmann et al., 2013). The observed decline in locomotion speed is
362 caused by different mechanisms. The photoactivation of ChR2 in GABAergic neurons induces a flaccid paralysis,
363 during which worms straighten up completely for a few seconds (Liewald et al, 2008). This observation is
364 consistent with the inhibitory role of GABA in the neuromuscular system. Stimulation of cholinergic neurons, on
365 the other hand, causes a spastic paralysis during which worms display dorsal coiling behavior in addition to body-
366 wall muscle contraction (Liewald et al., 2008; Kittelmann et al., 2013). This coiling behavior can be quantified by
367 following changes in eccentricity. Eccentricity is used as a measure of how nearly circular an ellipse is. Typically,
368 crawling and thrashing worms have an average eccentricity close to 0.93 or higher. At the same time, extreme
369 coilers can have an average eccentricity close to 0.6-0.7 (Koopman et al., 2020).

370 In liquid, photo-stimulation of ChR2 in GABAergic neurons inhibits swimming behavior, quantified as
371 the decline in trashing frequency (Liewald et al., 2008). The exact effects of cholinergic stimulation on swimming
372 behavior, however, still need to be determined. Both swimming behavior and coiling behavior in liquid can be
373 assessed with the WF-NTP (Koopman et al., 2020), allowing other readouts, in addition to changes in body length,
374 to be collected. Therefore, we analyzed thrashing frequency and eccentricity of worms in liquid expressing ChR2
375 under the *unc-17* or *unc-47* promotor to evaluate population-based optogenetic experiments with the OptoArm
376 and the WF-NTP (Figure 8A). We first explored the thrashing ability of worms grown with and without ATR
377 before and during photo-stimulation. Photoactivation of ChR2 causes a decrease in thrashing behavior independent
378 of which neuron-population was stimulated (Figure 8B). The kinetics of the observed movement-decline was
379 however strikingly different (Figure 8C). GABAergic stimulation causes an initial decrease in thrashing behavior
380 that gradually fades back to normal levels, while the cholinergic effect appears to saturate at the end illumination-
381 period (Figure 8C). Indeed, it has been shown before that worms recover partially from paralysis even tough
382 illumination of GABAergic ChR2 is sustained (Liewald et al., 2008). Taking this difference in kinetics into
383 account, we only analyzed the first 10 seconds of the movies for the worms with GABAergic ChR2-expression
384 and the last 10 seconds for worms with cholinergic ChR2-expression (Figure 8D). While the decline in thrashing
385 behavior was already evident and significant when complete movies were analyzed (Figure 8B), the effect was
386 more pronounced when taking the underlying kinetics into account (Figure 8D). Clearly, the population effect for
387 GABAergic stimulation is most prominent directly after photo-stimulation while the cholinergic system requires

388 more time for saturation of the effect. Importantly, at a blue-light intensity of 1 mW/mm^2, photoactivation of ChR2
389 in cholinergic-neurons does not result in complete paralysis of worms in liquid (Figure 8B-D). However, we did
390 observe clear decreases in eccentricity when cholinergic neurons were stimulated via ChR2-based illumination
391 (Figure 8E), while the eccentricity was unchanged after GABAergic stimulation or when worms were grown
392 without ATR (Figure 8E,F). Again, we did observe that this effect could be maximized by long-term stimulation
393 and analysing the last 10-seconds of the assay. Interestingly, coiling behavior upon cholinergic stimulation has
394 been ascribed to the concomitant GABA release that is indirectly triggered by photoactivation of cholinergic
395 neurons innervating GABAergic neurons (White et al., 1986; McIntire et al., 1993; Schuske et al., 2004; Liewald
396 et al., 2008). Coiling behavior is completely absent when GABAergic mutants expressing ChR2 in cholinergic
397 neurons are illuminated (Liewald et al., 2008). Therefore, coiling behavior likely provides a readout of the interplay
398 between GABAergic and cholinergic neurons within the nervous system.

399 Finally, we investigated the use of multi-worm illumination and low-resolution (e.g. perimeters of 60-80
400 pixels instead of 2000-3000 pixels) videos to calculate the body length of illuminated worms expressing ChR2
401 cholinergically. While the variation between individual worms was much larger when multiple worms were
402 illuminated at the same time, the average length of photoactivated worms was (0.92 ± 0.08) strikingly similar to
403 single-worm illumination (0.92 ± 0.02) (Figure 8G). The variation is most likely caused by the lack of flat-field
404 illumination of the OptoArm and thus, while being small, spatial differences in light intensity (Figure 3 and 4).
405 Taken together, combining the OptoArm with a multi-worm tracker provides a way to perform population-based
406 optogenetic experiments with multiple readouts in addition to body length. The coiling behavior and thrashing
407 capacity are examples of such readouts and provide distinct information about the functionality of the
408 neuromuscular system. However, it should be underlined that many other behaviors and associated readouts can
409 be assessed when ChR2 is expressed in different neuronal populations, e.g., crawling speed for food-slowing
410 (Sawin et al., 2000; possible with the WF-NTP), reversals for touch-neuron stimulation, egg-laying behavior after
411 HSN-stimulation (Leifer et al., 2011) and so on.

412

413 **A comprehensive optogenetic analysis reveals a faster age-dependent deterioration in the**
414 **cholinergic system compared to other components of a neuromuscular unit**

415 The ability to explore neuronal function with optogenetic tools provides an elegant way to study synaptic
416 connectivity and function. As animals age, they exhibit a gradual loss in motor activity (Hosono et al., 1980;
417 Bolanowski et al., 1980; Johnson et al., 1987; Herndon et al., 2002; Huang et al., 2004). Over the years, the hunt

418 for the mechanisms underlying this age-associated decline in movement have been subject to many studies
419 (Hosono et al., 1980; Bolanowski et al., 1980; Johnson et al., 1987; Herndon et al., 2002; Mulcahy et al., 2003;
420 Huang et al., 2004; Liu et al., 2013). For a long time, it has been hypothesized that the age-dependent decline in
421 motor activity is the result of muscle frailty rather than a functional deficit in the nervous system (Herndon et al.,
422 2002). This hypothesis was strengthened by studies showing that the structural integrity of the nervous system was
423 found to be well preserved over time (Dillin et al., 2002; Herndon et al., 2002; Huang et al., 2004; Murakami et
424 al., 2005; Hsu et al., 2009; Kauffman et al., 2010). When other studies described mild morphological deteriorations
425 at synapses at a later age, it was argued that the nervous system also undergoes are-related changed at the
426 morphological level (Pan et al., 2011; Tank et al., 2011; Toth et al., 2012). In 2013, Liu et al questioned whether
427 morphological analysis would be a reliable predictor for the functional status of a tissue. They showed that despite
428 the preservation of integrity, motor neurons undergo an age-related decline in function already starts in early life.
429 At the same time, such a functional decline was absent in body-wall muscles. Thus, they showed that neuronal
430 dysfunction precedes muscle dysfunction (Liu et al., 2013).

431 While Liu et al., (2013) shed light on the dynamics between the neuronal and muscle system during
432 ageing, they did not specifically focus on the different types of motor neurons. As mentioned earlier, movement
433 in *C. elegans* is the outcome of an antagonistic interplay between GABAergic inhibition and cholinergic
434 stimulation (McIntire et al., 1993; White et al., 1986). The lack of GABAergic input has severe consequence for
435 the movement capacity (Jiang et al., 2005; Tien et al., 2020), while increased GABAergic stimulation has also
436 been shown to results in cessation of thrashing behavior (Liewald et al., 2008; Figure 8). Clearly, the delicate
437 balance between excitation and inhibition determines the capacity to move. While electrophysiology is technically
438 challenging, optogenetics provide a relatively easy way of follow specific neuron populations functionally over
439 time and relate those readouts with behavioral changes. Here, we investigated the age-related decline of both
440 GABAergic neurons and cholinergic neurons specifically and correlated this decline with the deterioration of
441 movement (Figure 9A).

442 We started with assessing the movement decline over time by looking at the thrashing frequency of worms
443 expressing ChR2 under the *unc-17* or *unc-47* promotor. As expected, we observed a significant age-dependent
444 decline in thrashing frequency that is independent of the genotype (Figure 9B). In order to study the relation
445 between neuronal function and thrashing frequency, we assessed the 'Δ body length' of worms expressing ChR2
446 under the *unc-17* or *unc-47* promotor (e.g. elongation and contraction for GABAergic and cholinergic stimulation
447 respectively) as read-out for neuronal function after optogenetic stimulation with the OptoArm (1.6 mW/mm^2)

448 (Figure 9C). Subsequently the same worms were analyzed with the WF-NTP to assess their thrashing frequency
449 (Figure 9D). Different worms from the same population were tested at D1, D4, D8 and D11 of adulthood. Worms
450 expressing ChR2 under the *myo-3* promotor were included as a control for 'Δ body length'. As previously
451 described, we found that the postsynaptic muscle cells were relatively resistant to a functional decline in early life
452 (Figure 9C, Liu et al., 2003). The cholinergic neurons, however, revealed an almost logistic decline in function.
453 Strikingly, this decline was not observed in GABAergic neurons (Figure 9C). Then, we related the decline in
454 thrashing frequency (Figure 9D) with the decline in neuronal functioning (Figure 9C) for each genotype (Figure
455 9E). While the functional decline of neurons in neither of the motoneuron populations correlated perfectly with
456 the decline in thrashing frequency, the cholinergic neurons had a slope of almost 1, suggesting a strong relationship
457 between the decline in locomotion and neuronal function (Figure 9E). Notice that the curve is slightly right-shifted
458 ($y = ax + b$, $b = -0.267$), which implies that, even though the x, y relationship is almost 1.0 ($x \sim y$), a portion of the
459 decline in motility cannot be explained by cholinergic deterioration alone. Therefore, our data suggests that
460 cholinergic-dysfunction correlates best with the age-dependent movement deficits. At the same time, we show
461 evidence for different ageing kinetics between the cholinergic and GABAergic motorneurons. GABAergic neurons
462 appear more resilient to ageing, suggesting that not all *C. elegans* motoneurons age equally fast.
463 Since a delicate balance between GABAergic and cholinergic function is essential for movement, the
464 disbalanced decay between the two-neuron population might contribute to a changed excitation-to-inhibition ratio
465 to the muscle. As stated before, due to the wiring of the nervous system stimulation of cholinergic neurons
466 normally causes a concurrent activation of GABAergic neurons, that results in typical coiling-behavior (McIntire
467 et al., 1993; White et al., 1986; Schuske et al., 2004; Liewald et al., 2008; Figure 8), and provides a readout that
468 captures both systems at once. Therefore, we hypothesized that a changed balance between the GABAergic and
469 cholinergic system can translate into a changed light-induced coiling propensity. In order to tackle this question,
470 we assessed the change in eccentricity (as a readout for coiling propensity) induced by illumination of worms
471 expressing ChR2 in their cholinergic neurons at D4 and D8, just before and after the steep decline of the cholinergic
472 output (Figure 9C). Although not significant, we observed a clear and consistent increase in 'Δ eccentricity' at D8
473 compared to D4 (Figure 9F). The decrease in eccentricity is almost twice as high (*Cohen's d*: 1.99) at D8. In
474 conclusions, we hypothesize that the observed increase in coiling propensity could be due to an inequal decline of
475 cholinergic and GABAergic neurons and thus might provide a subtle hint for a changed excitation-to-inhibition
476 ratio towards inhibition.
477

Automation and additional features can further increase the ease of use and functionality of the OptoArm

All optogenetic data collected in this paper, was created with rather long photostimulation of at least 3 seconds. Those time-intervals can be relatively well established by manual operation of the OptoArm, e.g., using the ON-OFF switch. The manual OptoArm can definitely be valuable for acquiring consistent optogenetic data as is evidenced by all data that is described in this paper (Figure 7-9), but its consistency is highly operator-dependent. Moreover, it is practically impossible to generate the short-pulses or even high frequency trains required for certain experiments through manual operation (Liewald et al., 2008; Crawford et al., 2020). Therefore, we explored the use of a microcontroller to circumvent the use of a computer and to provide a low-cost solution to the aforementioned problems. The 700 mA externally dimmable BuckPuck DC driver that is used to power the LED, has a built-in 5V reference/output to directly power the logic circuitry of a μprocessor without the need for an additional power source (Figure 10A, Table 1). We used an Arduino uno as a microcontroller to control the output of the OptoArm, making it a stand-alone system. By connecting a pulse-width control pin (PWC, pin 9) to the CTRL pin of the driver, the Arduino cannot only control the duration of a light-pulse and the number of cycles, but can also adjust the light intensity, replacing the potentiometer (Figure 10B). These three parameters are easily adjustable by reprogramming of the Arduino software. However, adjusting Arduino scripts requires both knowledge of the programming language and a computer. Since we have tried to keep the OptoArm a standalone set-up that can be easily operated without specialistic knowledge and expensive equipment, we propose a more elegant solution. We decided to use an LCD-shield on top of the Arduino to adjust different parameters in live-modus without the intervention of a computer (Figure 10C). Then, we created an Arduino-script that allows users to use the LCD screen and connected buttons to select different options and menus (Supplementary software 1, Table 3, box 2). The software provides 3 programs through which the users can navigate for different experimental purposes: a testing program, a single run menu and a series pulse menu (Figure 10D,E, box 2). When using the automated OptoArm, one has to build the circuitry depicted in Figure 10A and upload the provided software to the Arduino only once (connect the CTRL pin of the LED driver to pin 9 of the Arduino to ensure compatibility between the software and the circuit). The used LCD-shield is relatively expensive when compared to the other components of the system, but it offers a user-friendly solution (Table 3, box 2). Nevertheless, other LCD screens can be used without a problem, as long as the software is adjusted as well.

It has been underlined now several times that the OptoArm provides the user with an adaptable system for optogenetic experiments. The ease of automating the OptoArm strengthens that statement, but there is more to

add. First of all, the system uses a royal-blue LED because ChR2 requires a wavelength in the blue spectrum. There are however many more, inhibitory light-gated ion pumps or outward-directed proton pumps that can be used for optogenetic purposes (Ihara et al., 1999; Waschuk et al., 2005; Zhang et al., 2007; Chow et al., 2010; Husson et al., 2012a). The yellow-green light-sensitive archaerhodopsin-3 (Arch) (Ihara et al., 1999), halorhodopsin from Natronomonas pharaonic (NpHR) (Zhang et al., 2007; Husson et al., 2012a) and rhodopsin from Leptosphaeria maculans (Mac) (Chow et al., 2010; Waschuk et al., 2005), are a few examples of the light-sensitive actuators that are widely used. NpHR, Arch and Mac are activated by wavelengths of 580-600 nm, 568 mm and 540 nm respectively (Husson et al., 2012a). By substituting the Royal Blue (448 nm) LED with a lime variant (567 nm), the OptoArm can also be used to photoactivate those inhibitory rhodopsins (Table 1). If one would be interested in switching between colors, we highly recommend to either built two arms, or to wire the OptoArm in such a way that only the heatsink and the attached LED can be disconnected and exchanged. Finally, while the OptoArm was specifically developed to work with *C. elegans*, it can also be used for experiments with *Drosophila melanogaster*. At present, required intensity for optogenetic stimulation of *D. melanogaster* is nowadays a few orders of magnitudes smaller. Commonly used intensities range from 50 uW/mm^2 to 0.3 mW/mm^2, although much higher intensities (<6.5 mW/mm2) are also used (Pulver et al., 2009; Dawydow et al., 2014; Meloni et al., 2020). To gain such small intensities with the OptoArm, one can use the systems intensity control, omit the use of lenses and/or increase the working-distance. In addition, with such a high sensitivity to light the effect of the backlight of recording systems (e.g. microscope and tracker lights) should be investigated as well.

Discussion

While pharmacological tools and electrophysiology provide an unprecedented way to analyze synaptic function in *C. elegans,* optogenetic tools have revolutionized the way we can study neuronal circuits in a more non-invasive way (Husson et al., 2013). The expression of light-sensitive ion channels and pumps under tissue or cell-specific promotors, allow researchers to remotely modify and manipulate the behavior of excitable cells (Nagel et al., 2003; 2005; Li et al., 2005; Schroll et al., 2006; Bi et al., 2006; Ishizuka et al., 2006; Zhang et al., 2007; Fang-Yen et al., 2015; Husson et al., 2013). Consequently, the ability to tweak synaptic activity and concurrently observe its effect on behavioral readouts, makes it possible to dissect the neuronal circuits underlying animal behavior. While many systems are available for optogenetic purposes (Weissenberger et al., 2011; Leifer et al., 2011; Stirman et al., 2010; 2011; Pulver et al., 2011; Husson et al., 2012b; Kawazoe et al., 2013; Qiu et al., 2015; Rabinowitch et al., 2016b;

538 2016a; Gengyo-Ando et al., 2017; Pokala et al., 2018, Crawford et al., 2020) the associated costs, the required
539 manual adaptations, compromises for usability and low adaptability provide a major bottleneck in the selection of
540 the system. Here, we argue that optogenetics should be made accessible to all researchers regardless of limited
541 financial resources or advanced technical expertise. Therefore, we designed a low cost optogenetics system that
542 provides high quality and consistent experiments, while also being easy and flexible in useability.

543 We have developed the OptoArm as an inexpensive and simple to setup system for the optogenetic
544 stimulation of *C. elegans*. It provides the user with adjustable light-intensity and lightning profiles via the
545 incorporation of interchangeable lenses. The ability to change lenses allows optogenetic manipulation and analysis
546 of the resulting behavior in both single worms and entire worm populations. Therefore, we technically validated
547 the system in different setups, ensuring compatibility with both standard microscopes and existing worm-trackers
548 like the WF-NTP. The compactness of the system makes it easy to incorporate in a variety of experimental setups,
549 as the only requirement is a power outlet and minimal space. In addition, the OptoArm can be easily automated
550 by the inclusion of a microcontroller, thereby allowing users to perform more complex optogenetic experiments
551 involving high-frequency trains of light-pulses. By offering both the option to build a manual and a fully automated
552 system, researchers are able to pick the set-up that fits their budget and requirements best. The cheapest version
553 of the OptoArm only costs $65 dollar, while the variant with an included stand will take about $ 90 dollars in total.
554 The fully automated system, including stand, is set to only ~ $128 dollar, thereby outperforming most other
555 optogenetic devises available. In addition, the capabilities of the system can be expanded by low-cost additional
556 modules as the need presents itself, making it an investment for the long-term as well.

557 Considering the fact that overall costs are often a key determinant in adopting a new device, the OptoArm
558 circumvents a major impediment. Next to its flexibility and adaptability, the OptoArm also bypasses the need of
559 extra adjustments that are often required for low-cost systems, like aluminum foil or closed boxes, which are often
560 incompatible with live imaging systems. Therefore, the OptoArm provides a way to illuminate and record worms
561 simultaneously. Nevertheless, there are also some disadvantages when comparing the OptoArm with more
562 expensive optogenetic systems (Leifer et al., 2011; Stirman et al., 2010; 2011; Weissenberger et al., 2011; Husson
563 et al., 2012b; Qiu et al., 2015; Rabinowitch et al., 2016a;;Gengyo-Ando et al., 2017; Busack et al., 2020). First of
564 all, the OptoArm does not allow to follow single worms in space with both temporal and chromatic precision. It
565 does not allow illumination at a specified anatomical position only. Therefore, it is not possible to excite single
566 neurons with the OptoArm. Nonetheless, this is only required for very specific, specialist applications. Secondly,
567 our current configuration of the OptoArm provides an adaptable light intensity between ~up till 1.8 mW/mm^2

568 (with a fixed working-distance of 3.5 cm), but some experimental procedures require a higher intensity up till 5
569 mW/mm^2 (Husson et al., 2013). However, it is possible to extend the system with a tri-LED that triples the power
570 of the available light. In this way, with the appropriate thermal management and lenses, the light intensity of the
571 OptoArm could be further increased. Thirdly, while it is possible to perform multi-worm illumination with the
572 OptoArm, the spatial consistency is not ideal. For plates requiring illumination of a small surface area (e.g., 3-cm,
573 12-wells), the OptoArm can provide a coverage of sufficiently consistent light intensity. Yet, when larger areas
574 are illuminated, the light-gradient and intensity drop towards the periphery becomes more of an issue. Lastly, the
575 OptoArm cannot shift between wavelengths, as would be possible with a fluorescence microscope. Nevertheless,
576 it is possible to change illumination color by incorporating different types of LEDs. In this way, the OptoArm
577 could not only be used for photoactivation of ChR2, but also for Mac, NpHR or Arch (Husson et al., 2012a).
578 Clearly, the modular nature of the OptoArm can be used to overcome some of the mentioned limitations.

579 While some disadvantages exist, we still demonstrated that the OptoArm can accurately reproduce
580 previously established findings that were acquired with more expensive optogenetic systems. Furthermore, by
581 using the OptoArm with the WF-NTP a variety of population characteristics can be acquired on both solid and
582 liquid media, despite some spatial inconsistency in illumination. We also show that the OptoArm can be used to
583 tackle novel questions by combining different optogenetic readouts. In fact, we used the OptoArm to study the
584 age-related decline of specific motor neurons and the accompanying deterioration in locomotion. We found a
585 striking correlation between the age-dependent decline in cholinergic output and the decline in thrashing capacity.
586 However, the decrease in cholinergic output, as evidenced by a change in body length upon optogenetic
587 stimulation, did not completely explain the drop in movement capacity during ageing. Neither did the decrease in
588 GABAergic output or muscle function. In fact, we observed that the muscular and GABAergic system appeared
589 to be more resilient to age-related deterioration. Indeed, the age-related decrease in GABAergic output was much
590 smaller than that of the cholinergic branch. It has been previously shown that the overall function of a
591 neuromuscular unit decreases early in life due to neuronal deficits rather than of muscle dysfunction (Liu et al.,
592 2013). However, to our knowledge, the striking differences in ageing-kinetics between GABAergic and
593 cholinergic neurons has not been described before.

594 The GABAergic and cholinergic system are inextricably linked and regulate the fine balance of
595 excitation-to-inhibition stimuli to the muscle, ensuring coordinated movement. (White et al., 1986; McIntire et al.,
596 1993). If GABAergic neurons are indeed more resilient to ageing, while cholinergic neurons gradually lose their
597 functional capacity, the balance of the excitation-to-inhibition ratio for muscle cells might also change.

598 Intriguingly, given the underlying interaction between GABAergic and cholinergic neurons that shapes the coiling
599 phenotype (Liewald et al., 2008), the observed light-induced increase in coiling behavior at later ages might
600 actually provide the first hint for an altered excitation-to-inhibition ratio. While the age-dependent decline in
601 locomotion correlates well with a decrease in cholinergic signaling, it might be enhanced by the much slower
602 decline in GABAergic function. To add another layer of complexity, a study by Liu et al. (2013) found evidence
603 of postsynaptic sensitization, increasing the amplitude of both acetylcholine- and GABA-evoked muscle currents
604 during early ageing and peaking at D9. The relationship between these postsynaptic adaptation mechanisms and
605 presynaptic changes will further determine the delicate balance of the neuromuscular unit and the overall
606 movement capacity. Clearly, further research to unravel the complex interplay that contributes to age-related
607 decrease in movement capacity is required and should integrate all these components instead of focusing on a
608 single compartment. Moreover, comparing GABAergic and cholinergic neurons molecularly might provide insight
609 into the key players underlying the differences in resilience to ageing.
610 In conclusion, we have presented here a low-cost, easy-to-build and highly adaptable optogenetic device
611 that allows researcher to perform novel optogenetic experiments with *C. elegans* and other small organisms. We
612 validated the OptoArm technically and biologically in different set-ups for both single and multiple worm
613 experiments. The flexible and adaptable nature ensures compatibility with different recording systems, allowing
614 different readouts to be combined for more elaborate insight in biological systems. The OptoArm can be easily
615 operated without expert knowledge and, due to its modular nature and cheap components, can be easily adapted
616 as well. In the end, users have ultimate control over their budget and system configuration. Altogether, we show
617 that the OptoArm is able to overcome some of the major obstacles preventing a more wide-spread implementation
618 of optogenetics, including in teaching institutes.
619

620 # Materials and methods

621 **Strains and maintenance**

622 Standard conditions were used for *C. elegans* propagation at 20 ºC (Brenner, 1974). Animals were synchronized
623 by hypochlorite bleaching, hatched overnight in M9 buffer and subsequently cultured on NGM agar plates seeded
624 with OP50. For optogenetic experiments, transgenic worms were cultivated in the dark at 20 ºC on NGM plates
625 with or without 0.2 mM all-trans retinal (ATR) added to the OP50. A final concentration of 0.2 mM ATR was
626 obtained by mixing 0.4 ul of a 100 mM ATR stock solution in ethanol (Sigma-Aldrich) with the 200 uL E. coli
627 that was spread on each 6 cm plate. For ageing experiments, worms were transferred ~72 hours after plating to

628 NGM plates containing 5-Fluoro-2'deoxy-uridine (FUdR) to inhibit growth of offspring. For ageing experiments
629 untill adulthood D12, worms were transferred every 3 days to fresh ATR+ and ATR- plates. The following
630 genotypes were used: ZX388: zxIs3[*unc-47p::ChR2(H134R)::YFP + lin-15(+)]*V, ZX460: zxIs6[*unc-*
631 *17p::ChR2(H134R)::YFP + lin-15(+)*]V, ZX463: *unc-47(e307)*III; *zxIs3*, ZX465: *unc-26(s1710)*IV; *zxIs3*,
632 ZX511: *unc-26(s1710)*IV; *zxIs6*, ZX531: *unc-47(e307)*III; *zxIs6*. All strains were a kind gift of professor A.
633 Gottschalk.
634

635 **The OptoArm**

636 *Required components.* All the components of the Optoarm are by Quadica Developments, unless stated differently.
637 For the electronic circuitry we refer to Figure 2A. The OptoArm consists of a Royal-Blue (448nm) Rebel LED
638 on a SinkPAD-II 20 mm Star Base of 1.03 W (SP-01-V4), powered by a 700 mA externally dimmable BuckPuck
639 DC driver – with leads (3023-D-E-700), and connected to a connecting wire with adjustable potentiometer of 5
640 kΩ (3021HEP). The LED is attached to a heatsink (50 mm Round x 44 mm high alpha heat sink – 5.2 °C/W;
641 CN50-40B) with pre-cut thermal adhesive tape for 20 mm Star LED assemblies (LXT-S-12). The lens-holder was
642 self-manufactured from aluminum with a Schaublin 125 lathe (ϕ21 mm, inner circle) and contains a small screw-
643 hole at the side (M2) for tightening and loosening lenses and two grooves for the LED-wires (Figure 2B). The
644 holder was attached to the heat sink with mounting tape for kathod 20 mm Round optic Holders (LT-06). Three
645 different lenses (with adjacent integrated holder) were used: Khatod 10° 22mm circular beam optic (KEPL115406
646 by Khatod Optoelectronic), Fraen 21° 22 mm circular beam optic (FLP-M4-RE-HRF, by Fraen Corporation),
647 Khatod 40° 22 mm circular beam optic (KEPL115440 by Khatod Optoelectronic). For the ON/OFF switched a
648 latching pressure switch (≤3A, ≤ 250V; Velleman – R1821A-RD) was used. The whole system was mounted on
649 a three-pronged clamp (ϕ10 mm, 241-7432, Usbeck Carl Fried). A cross clamp (105 BR 10, Comar) was placed
650 on the rod of the clamp. The clamp provides a way to fixate a standard DC contra plug (≤4A, ≤25 V, Velleman;
651 CD021) and to power the system with a DC-adapter. Due to the nature of a LED driver, the input voltage to the
652 driver must always be higher than the total forward voltage drop of all connected and consuming components. In
653 this case, the driver has a minimal input margin of 2.5 V and the LED consumes about 3.5 V, leading to a minimal
654 input voltage of 6V. However, when working with a potentiometer it is highly recommended to use a minimum
655 of $7V_{DC}$ (as evidenced by the spec sheet). We have been using a $9V_{DC}$, $12V_{DC}$ and $15V_{DC}$ adapters (~ 1.0 – 1.2 A)
656 with good results. All components can also be found in table 1. Clearly, one can substitute the potentiometer,

switch and DC connector for cheaper variants. The critical parts of the system include the LED, heat-sink, and steady 700mA driver together with the lenses.

Automated OptoArm. For the automated OptoArm, the aforementioned components are extended with an Arduino Uno (or any clone), a capacitor of 0.1 uf (Xicon Ceramic Disc Capacitors; Mouser electronics, 140-50U5-204M-RC) and an LCD Shield kit w/ 16x2 character display (Adafruit, ID:714), while the connecting wire with adjustable potentiometer of 5 kΩ can be omitted. The shield has to be assembled with some soldering-steps; a great tutorial can be found here: https://learn.adafruit.com/rgb-lcd-shield/assembly. See Figure 10A for the electronic circuitry. The accompanying Arduino code for the LCD-shield is freely available and can be downloaded from: Supplementary Software 1 (the software runs under the license of Attribution-NonCommercial-ShareAlike 4.0 International (CC BY-NC-SA 4.0). When using this software, connect pin D9 of the Arduino to CTRL pin of the LED driver.

Stands. For experiments with the WF-NTP, we used a stand that was built with the following components: stand rod (1000 mm, ϕ12 mm, 241-7153, Usbeck Carl Fried), double bosshead (241-7104, Usbeck Carl Fried), retort stand base, tripod (241-0245, Usbeck Carl Fried). For experiments with a microscope, we used a stand with the following components: basic carrier (20 RM 01, Comar), Pinion stage (30 XT 40), post-holder (45 BH 10), rod (203 RM 01), self-manufactured base.

Microscope and WF-NTP setup

Microscope: a high-resolution microscopy system was used to image the worms, consisting of an Olympus SZ51 microscope coupled with an IphoneX via a Carson HookUpz 2.0. smartphone adapter. The UV-protection shield of a Leica MZ 16 FA was used to avoid saturation of the camera. In general, a 1.7x digital zoom (of the Iphone) was used in combination with a 15-30x magnification of the microscope, and videos were always acquired with a framerate of 30 fps. Actual working distances were determined by measuring the height from the surface perpendicular to the middle of the LED and using the trigonometric ratio for sine, eq. 9, to calculate the length of the hypotenuse side:

$$\mathbf{sin}(\boldsymbol{\theta}) = \frac{\boldsymbol{opposite}}{\boldsymbol{hypotenuse}} \quad (9)$$

A working-distance of 3.5 cm is often adequate. WF-NTP: the used set-up was identical to the one described in Koopman et al., (2020), using a camera-to-sample distance of 140 mm. The used framerate was always 20 fps and the working-distance was set to ~ 4.1 cm. In both set-ups, light intensity was always measured at 448 nm with a M16-130 USB power meter (Thorlabs, ϕ 9.5 mm) to verify the required conditions. Before each experiment we measured the light-intensity to ensure appropriate conditions, assuming a Gaussian light source (in the software).

Behavioral experiments

For single-worm illumination, worms were freely moving on unseeded 3-cm NGM plates and kept in frame by manual location. For 'short-term' experiments, worms were exposed to a 3-3-3 lightening regime, in which light was OFF for 3 seconds, followed by light ON for 3 seconds and light OFF for another 3 seconds. Light intensity was always 1.6 mW/mm^2 (10° lens) unless stated differently. For 'long-term' experiments, worms were exposed to a 1-50-1 lightening regime in which light was OFF for 1 seconds, followed by light ON for 50 seconds and light OFF for another second. For multiple-worm illumination, worms were collected in M9 buffer and plated on an empty 3-cm plate that was flooded with 1.5 mL M9. Worms were recorded with the WF-NTP set-up at a framerate of 20 fps and a light intensity of 1.0 mW/mm^2 (21° lens) unless stated differently. We generated separate movies for light OFF (30 seconds) and light ON (30 seconds). For most experiments, as for the ageing-timeline, worms were first examined via single-worm illumination and subsequently transferred to M9 for multi-worm illumination.

Image processing

Videos of multiple-worm illumination, acquired with the WF-NTP platform, were analyzed with accompanying software as described in Koopman et al., 2020. Videos that were acquired with a cell-phone (Iphone X) were transferred to a computer (.mov) and first converted to ImageJ compatible files (.avi) with ffmpeg. We used a terminal (cmd for Windows, terminal for MacOS) to navigate to the directory with the movies and quickly convert multiple movies. When opening a terminal, the current location will be visible (e.g., C:\Users\). When the movies are saved at a different disk, for example, D, one can use the command: `C:\Users\Tracker>d:` followed by pressing 'Enter' to switch directly to that disk. Paths can be removed with the command **`cd\`**, for example, `C:\Users\Movies>cd\` followed by pressing 'Enter'. This will yield '`C:\Users`'. Adding paths is managed by typing `cd X`, for example, `C:\>cd Movies` followed by pressing 'Enter'. This will yield '`C:\Movies`. When the appropriate directory is selected, the following command can be executed:

```
for i in *.MOV; do ffmpeg -i "$i" -pix_fmt nv12 -f avi -vcodec rawvideo
"${i%.*}.avi"; done
```

This code converts all .MOV files in the directory to .AVI files at the same time. For the perimeter-approach, the converted movies were processed with ImageJ. Movies were first set to an 8-bit format (Image > Type > 8-bit) and then duplicated (Image > Duplicate) to ensure accessible images for all subsequent steps. Next, the movie contrast was enhanced by selecting 0.3% saturated pixels and normalized enhancement (Process > Enhance), followed by background subtraction with a rolling ball radius of 50 px (Process > Subtract Background). Then, we thresholded the images (Image > Adjust > Threshold) by the Huang method (same threshold for the wole stack) and applied the settings to all frames. Finally, we measured the perimeter of the worm per frame by setting the measurements (Analyze > Set measurements) to perimeter only and clicking on 'analyze particles' (Analyze > Analyze particles). One should set a lower-limit of the size of the particles to avoid noise being picked up. This number highly depends on the used magnification and should therefore be determined by an empirical approach. We recommend to record the first processing steps until subtracting the background (Plugins > Macros > Record) and created a macro (Create) that can be rerun for every movie. In this way, only the thresholding had to be performed manually. Measurements were normalized by the average pixel length of the perimeter measured in the first 30-60 frames (light OFF). For long-term experiments, a midline approach was used at specified intervals (0.5 seconds, 2 seconds, 10 seconds, 20 seconds, 30 seconds, 40 seconds, 50 seconds and 52 seconds). If the midline approach was used for short-term experiments, we measured the body-length 500 ms before light was ON and 1000 ms after light was turned ON. When the midline-approach is specifically mentioned, we measured the body length by drawing a midline from head to tail with a drawing-tablet (Wacom).

Statistics and visualization

Statistical analyses were done in R and Graphpad Prism 8. The used statistical tests can be found in the different figures and are based on several criteria. In short, (log-)normality tests were always performed on the collected data to test for gaussian distributions (e.g. Shapiro-Wilk). Based on the distribution of the data the appropriate test was selected (parametric or non-parametric). When more than two groups were compared, multiple-testing correction was always applied. When inequality of variance was expected between two groups (based on the experimental design) student's t-test were always performed with a Welsch's correction (The Welch test must be specified as part of the experimental design, and not decided upon *a posterori;* Moser et al., 1992; Hayes et al.,

2007). Post-hoc testing after a one- or two-way ANOVA was only performed when the initial test gave significant results. All experiments were replicated three times, unless stated differently. *: $p \leq 0.05$, **: $p \leq 0.01$, ***: $p \leq 0.001$. All data was visualized with R (ggplot2) or Graphpad Prism 8 and color-adjusted in Adobe Illustrator. Integrated intensity plots were created with R, by applying a general LOESS model on the measured point to estimate/interpolate the intensities at the non-measured coordinates.

Acknowledgements

We thank Alexander Gottschalk for kindly sharing several strains and fruitful tips and trick on optogenetics with *C. elegans*. This project was funded by a BCN-Brain grant (to M.K.) and a grant of Stichting ALS Nederland (to E.E.A. and M.K.)

Author contributions

L.J. and M.K. designed and built the OptoArm together. M.K. performed all technical and biological experiments, analyzed and visualized them. L.J. wrote the accompanying Arduino script. M.K. wrote the manuscript with input from L.J. and E.A.A.

Conflict of Interests

The authors declare that they have no conflict of interest.

References

Almedom R.B. Liewald J.F., Hernando G., Schultheis C., Rayes D., Pan J., Schedletzky T., Hutter H., Bouzat C., Gottschalk A. 2009. An ER-resident membrane protein complex regulates nicotinic acetylcholine receptor subunit composition at the synapse. *EMBO J.* **28**, 2636–2649.

Antoscheckin, I., Sternberg, P.W. 2007. The versatile worm: genetic and genomic resources for *Caenorhabditis elegans* research. *Nat. Rev. Genet.* **8**:518-532.

Aravamudan B., Fergestad T., Davis W.S., Rodesch C.K., Broadie K. 1999. *Drosophila* UNC-13 is essential for synaptic transmission. *Nat. Neurosci*. ***2***, 965–971.

Augustin I., Rosenmund C., Sudhof T.C., Brose N. 1999. Munc13-1 is essential for fusion competence of glutamatergic synaptic vesicles. *Nature* **400**: 457–461.

Betz A., Ashery U., Rickmann M., Augustin I., Neher E., Sudhof T.C., Rettig J., Brose N. 1998. Munc13-1 is a presynaptic phorbol ester receptor that enhances neurotransmitter release. *Neuron* ***21***, 123–136.

Bi A., Cui J., Ma Y-P., Olshevskaya E., Pu M., Dizhoor A.M., Pan Z-H. 2006. Ectopic expression of a microbial-type rhodopsin restores visual responses in mice with photoreceptor degeneration. *Neuron* **50**: 23–33.

Bolanowski M.A., Russell R.L., Jacobson L.A. 1981. Quantitative measures of aging in the nematode *Caenorhabditis elegans*. I. Population and longitudinal studies of two behavioral parameters. *Mech. Ageing Dev.* **15**: 279–295

Brenner S. 1974. The genetics of Caenorhabditis elegans. *Genetics*, **77**(1): 71-94.

Brose N., Hofmann K., Hata Y., Sudhof T.C. 1995. Mammalian homologues of *Caenorhabditis elegans* unc-13 gene define novel family of C_2-domain proteins. *The Journal of Biological Chemistry*, **270**(42): 25273-25280.

Busack I., Jordan F., Sapir P., Bringmann H. 2020. The OptoGenBox – a device for long-term optogenetics in *C. elegans*. *Journal of Neurogenetics,* **34**(3-4): 466-474.

Busch K.E., Laurent P., Soltesz Z., Murphy R.J., Faivre O., Hedwig B., Thomas M., Smith H.L., de Bono M. 2012. Tonic signaling from O(2) sensors sets neural circuit activity and behavioral state. *Nat. Neurosci*. **15**: 581–59.

Chow B.Y., Han X. Dobry A.S., Qian X., Chuong A.S., Li M., Henninger M.A., Belfort G.M., Lin Y., Monahan P.E., Boyden E.S. 2010. High-performance genetically targetable optical neural silencing by light-driven proton pumps. *Nature*, **463**: 98-102.

Crawford Z., San-Miguel A. 2020. An inexpensive programmable optogenetic platform for controlled neuronal activation regimens in *C. elegans*. *APL bioengineering*, ***4***(1): 016101.

Dalapati P., Manik N.B., Basu A.N. 2016. Effect of temperature on the opto-electrical properties of GaP based light emitting diodes. *Optik*, **127**: 2598-2602.

Dawydow A., Gueta R., Ljaschenko D., Ullrich S., Hermann M., Ehmann N., Gao S., Fiala A., Langenhan T., Nagel G., Kittel R.J. 2014. Channelrhodopsin-2-XXL, a powerful optogenetic tool for low-light applications. *Proc. Natl. Acad. Sci. U.S.A.* **111**(38): 13972-13977.

Dillin A., Hsu A.L., Arantes-Oliveira N., Lehrer-Graiwer J., Hsin H., Fraser A.G., Kamath R.S., Ahringer J., Kenyon C. 2002. Rates of behavior and aging specified by mitochondrial function during development. *Science*. **298:** 2398–2401.

Fang S., Wang W., Liang J., Liang Z., Qin Y., Lv J. 2017. Heat dissipation analysis of bendable AlGalnP micro-LED arrays. *AIP Advances,* **7**: 015209.

Fang-Yen C., Alkema M.J., Samuel A.D. 2015. Illuminating neural circuits and behaviour in Caenorhabditis elegans with optogenetics. *Phil. Trans. R. Soc*. **370**(1677):20140212.

Faumont S., Rondeau G., Thiele T.R., Lawton K.J., McCormick K.E., Sottile M., Griesbeck O., Heckscher E.S., Roberts W.M., Doe C.Q., Lockery S.R. 2011. An image-free opto-mechanical system for creating virtual environments and imaging neuronal activity in freely moving *Caenorhabditis elegans*. *PLoS ONE* **6**: e24666.

Francis M.M., Maricq A.V. 2006. Electrophysiological analysis of neuronal and muscle function in *C. elegans*. *Methods Mol. Biol.* **351**: 175–192.

Francis M.M., Mellem J.E. and Maricq A.V. 2003. Bridging the gap between genes and behavior: recent advances in the electrophysiological analysis of neural function in *Caenorhabditis elegans*. *Trends Neurosci.* **26**: 90–99.

Franks C.J., Murray C., Ogden D., O'Connor V., Holden-Dye L. 2009. A comparison of electrically evoked and channel rhodopsin-evoked postsynaptic potentials in the pharyngeal system of *Caenorhabditis elegans*. *Invert. Neurosci*. **9**: 43–56.

Fu H., Zhao Y. 2018. Efficiency droop in GaInN/GaN LEDs. In *Nitride Semiconductor Light-Emitting Diodes (LEDs): Materials, Technologies, and Applications: Second Edition (pp. 299-325). Elsevier* 10.1016/B978-0-08-101942-9.00009-5.

Fujiwara M., Sengupta P., McIntire S.L. 2002. Regulation of body size and behavioral state of *C. elegans* by sensory perception and the EGL-4 cGMP-dependent protein kinase. *Neuron*, **36**(6): 1091-1102.

Gao, S., Zhen, M. 2011. Action potentials drive body wall muscle contractions in *Caenorhabditis elegans*. *Proc. Natl. Acad. Sci. U.S.A.* **108**: 2557–2562.

Geffeney S.L., Cueva J.G., Glauser D.A., Doll J.C., Lee T.H.-C., Montoya M., Karania S., Garakani A.M., Pruitt B.L., Goodman M.B. 2011. DEG/ENaC but not TRP channels are the major mechanoelectrical transduction channels in a *C. elegans* nociceptor. *Neuron* **71**: 845–857.

Gengyo-Ando K., Kagawa-Nagamura Y., Ohkura M., Fei X., Chen M., Hashimoto K., Nakai J. 2017. A new platform for long-term tracking and recording of neural activity and simultaneous optogenetic control in freely behaving Caenorhabditis elegans. *Journal of Neuroscience Methods*, **286**: *56–68.*

Goodman M.B., Hall D.H., Avery L., Lockery S.R. 1998. Active currents regulate sensitivity and dynamic range in *C. elegans* neurons. *Neuron,* **20**:763–772.

Goodman M.B., Lindsay T.H., Lockery S.R. and Richmond J.E. 2012. Electrophysiological methods for *Caenorhabditis elegans* neurobiology. *Methods Cell Biol.* **107**: 409–436.

Guo Z.V., Hart A.C., Ramanathan, S. 2009. Optical interrogation of neural circuits in *Caenorhabditis elegans*. *Nat. Methods,* **6**: 891–896.

Han N., Jung E., Han M., Ryu B.D., Ko K.B., Park Y.J., Cuong T.V., Cho J., Kim H., Hong C.H. 2015. Reduced junction temperature and enhanced performance of high power light-emitting diodes using reduced graphene oxide pattern. *Appl. Phys*. **48**: 265102.

Harris T.W., Hartwieg E., Horvitz H.R., Jorgensen E.M. 2000. Mutations in synaptojanin disrupt synaptic vesicle recycling. J. *Cell Biol.* **150**: 589–600.

Hayes A.F., Cai L. 2007. Further evaluating the conditional decision rule for comparing two independent means. *Br J Math Stat Psychol,* **60**(2): 217-244.

Herndon L.A., Schmeissner P.J., Dudaronek J.M., Brown P.A., Listner K.M., Sakano Y., Paupard M.C., Hall D.H., Driscoll M. 2002. Stochastic and genetic factors influence tissue-specific decline in ageing *C. elegans*. *Nature* ***419***:808–814.

Hope, I.A. 1999. Background on *Caenorhabditis elegans*. In: Hope I.A., editor. C. elegans: a practical approach. NY: Oxford University Press: 1-15.

Hosono R., Kamiya Y. 1991. Additional genes which result in an elevation of acetylcholine levels by mutations in *Caenorhabditis elegans*. *Neurosci Lett.* **128**:243–244.

Hosono R., Sassa T., Kuno S. 1989 Spontaneous mutations of trichlorfon resistance in the nematode *Caenorhabditis elegans*. *Zool Sci* **6**:697–708.

Hosono R., Sato Y., Aizawa S.I., Mitsui Y. 1980. Age-dependent changes in mobility and separation of the nematode *Caenorhabditis elegans*. *Exp. Gerontol.* ***15***: 285–289.

Hsu A.L., Feng Z., Hsieh M.Y., Xu X.Z. 2009. Identification by machine vision of the rate of motor activity decline as a lifespan predictor in C. elegans. *Neurobiol Aging.* **30**:1498–1503.

Huang C., Xiong C., Kornfeld K. 2004. Measurements of age-related changes of physiological processes that predict lifespan of *Caenorhabditis elegans*. *Proc. Natl. Acad. Sci. U.S.A.* **101**: 8084–8089.

Huang J., Golubovic D.S., Koh S., Yang D., Li X., Fan X., Zhang G.Q. 2015. Degradation Mechanisms of Mid-Power White-Light LEDs Under High-Temperature–Humidity Conditions. *IEEE Transactions on Device and Materials Reliability*, **15**(2): 220-228.

Husson S. J., Costa W. S., Wabnig S., Stirman J. N., Watson J. D., Spencer W. C., Akerboom J., Looger L. L., Treinin M., Miller D. M., Lu H., Gottschalk A. 2012b. Optogenetic analysis of a nociceptor neuron and network reveals ion channels acting downstream of primary sensors. *Curr. Biol.* **22**: P743.

Husson S.J., Gottschalk A., Leifer A.M. 2013. Optogenetic manipulation of neural activity in *C. elegans*: From synapse to circuits and behavior. *Biology of the Cell*, **105**(6): 235–250.

Husson S.J., Liewald J.F., Schultheis C., Stirman J.N., Lu H., Gottschalk A. 2012a. Microbial light-activatable proton pumps as neuronal inhibitors to functionally dissect neuronal networks in *C. elegans*. *PLoS ONE,* **7**: e40937.

Ihara K., Umemura T., Katagiri I., Kitajima-Ihara T., Sugiyama Y., Kimura Y., Mukohata Y.1999. Evolution of the archaeal rhodopsins: evolution rate changes by gene duplication and functional differentiation. *J Mol Biol,* **285:** 163-174.

Ishizuka T., Kakuda M., Araki R., Yawo H. 2006. Kinetic evaluation of photosensitivity in genetically engineered neurons expressing green algae light-gated channels. *Neurosci. Res.* **54**: 85–94.

Javer A., Ripoll-Sánchez L., Brown A.E.X. 2018. Powerful and interpretable behavioural features for quantitative phenotyping of *Caenorhabdities elegans*. *Philos Trans R Soc Lond B Biol Sci.* **373**(1758): 20170375.

Jiang G., Zhuang L., Miyauchi S., Miyake K., Fei Y-J., Ganapathy V. 2005. A Na+/Cl- coupled GABA transporter, GAT-1, from Caenorhabditis elegans. *Membrane transport, structure, function and biogenesis,* **280**(3): 2065-2077.

Johnson T.E. 1987. Aging can be genetically dissected into component processes using long-lived lines of *Caenorhabditis elegans*. *Proc. Natl. Acad. Sci. U.S.A.* **84**: 3777–3781.

Jorgensen E.M., Hartwieg E., Schuske K., Nonet M.L., Jin Y., Horvitz H.R. 1995. Defective recycling of synaptic vesicles in synaptotagmin mutants of *Caenorhabditis elegans*. *Nature,* **378**:196–199.

Kaletta T., Hengartner M.O. 2006 Finding function in novel targets: *C. elegans* as a model organism. *Nature Reviews Drug Discovery,* **5**: 387-399.

Kammenga J.E., Doroszuk A., Riksen J.A.G., Hazendonk E., Spiridon L., Petrescu A-J., Tijsterman M., Plasterk R.H.A., Bakker J. 2007. A Caenorhabditis elgans wild type defies the temperature-size rule owing to a single nucleotide polymorphism in tra-3. *PLOS Genetics,* **3**(3): e34.

Kang L., Gao J., Schafer W.R., Xie Z., Xu X.Z.S. 2010. C. elegans TRP family protein TRP-4 is a pore-forming subunit of a native mechanotransduction channel. *Neuron,* **67**: 381–391.

Kauffman A.L., Ashraf J.M., Corces-Zimmerman M.R., Landis J.N., Murphy C.T. 2010. Insulin signaling and dietary restriction differentially influence the decline of learning and memory with age. *PLoS Biol*. **8**:e1000372.

Kawano T., Po M.D., Gao S., Leung G., Ryu W.S., Zhen M. 2011. An imbalancing act: gap junctions reduce the backward motor circuit activity to bias *C. elegans* for forward locomotion. *Neuron,* **72**: 572–586.

Kawazoe Y., Yawo H., Kimura K. D. 2013. A simple optogenetic system for behavioral analysis of freely moving small animals. *Neurosci. Res.* **75**: 65-68.

Kim D-S., Han B. 2016. Effect of junction temperature on heat dissipation of high power light emitting diodes. *Journal of Applied Physics,* **119**: 125104.

Kittelmann M., Liewald J.F, Hegermann J., Schultheis C., Brauner M., Steuer Costa W., Wabnig S., Eimer S., Gottschalk A. 2013. In vivo synaptic recovery following optogenetic hyperstimulation. *Proc. Natl Acad. Sci. USA,* **110**: E3007–E3016.

Kocabas A., Shen C-H., Guo Z.V., Ramanathan S. 2012. Controlling interneuron activity in *Caenorhabditis elegans* to evoke chemotactic behaviour. *Nature*, **490**: 273-277.

Kolbe M., Besir H., Essen L.O., Oesterhelt D. 2000. Structure of the light-driven chloride pump halorhodopsin at 1.8 Å resolution. *Science,* **288**: 1390–1396.

Koopman M., Peter Q., Seinstra R.I., Perni M., Vendruscolo M., Dobson C.M., Knowles T.P.J. Nollen E.A.A. 2020. Assessing motor-related phenotypes of *Caenorhabditis elegans* with the wide field-of-view nematode tracking platform. *Nat. Protoc.* **15**(6): 2071-2106.

Kwon N., Pyo J., Lee S.J., Je J.H. 2013. 3-D worm tracker for freely moving C. elegans. *PLoS One.* **8**(2): e57484.

Lackner M.R., Nurrish S.J., Kaplan J.M. 1999. Facilitation of synaptic transmission by EGL-30 Gqalpha and EGL-8 PLCbeta: DAG binding to UNC-13 is required to stimulate acetylcholine release. *Neuron* **24**: 335–346.

Lee D.H., Lee H.K., Yu J.S., Bae S.J., Choi J.H., Kim D.H., Ju I.C., Song K.M., Kim J.M., Shin C.S. 2011. Temperature and thermal characteristics of InGaN/GaN vertical light-emitting diodes on electroplated copper. Semicond. *Sci. Technol.* **26**: 055014.

Leifer A.M., Fang-Yen C., Gershow M., Alkema M.J., Samuel A.D.T. 2011. Optogenetic manipulation of neuronal activity in freely moving *Caenorhabditis elegans*. *Nat. Methods,* **8**:147–152.

Lewis J.A., Fleming J.T., McLafferty S., Murphy H. and Wu C. 1987. The levamisole receptor, a cholinergic receptor of the nematode *Caenorhabditis elegans*. *Mol. Pharmacol*. **31**: 185–193.

Li X., Gutierrez D.V., Hanson M.G., Han J., Mark M.D., Chiel H., Hegemann P., Landmesser L.T., Herlitze S. 2005. Fast noninvasive activation and inhibition of neural and network activity by vertebrate rhodopsin and green algae channelrhodopsin. *Proc. Natl Acad. Sci. USA,* **102**: 17816–17821.

Liewald J.F., Brauner M., Stephens G.J., Bouhours M., Schultheis C., Zhen M., Gottschalk, A. 2008. Optogenetic analysis of synaptic function. *Nat. Methods,* **5**: 895–902.

Lin Y., Lu Y., Gao Y., Chen Y., Chen Z. 2011. Measuring the thermal resistance of LED packages in pratical circumstances. *Thermochimica Acta*, **520**: *105-109.*

Lindsay T.H., Thiele T.R., Lockery S.R. 2011. Optogenetic analysis of synaptic transmission in the central nervous system of the nematode *Caenorhabditis elegans*. *Nat. Commun*. **2**: 306.

Liu J., Zang B., Lei H., Feng Z., Liu J., Hsu A-L., Xu X.Z.S. 2013. Functional aging in the nervous system contributes to age-dependent motor activity decline in *C. elegans*. *Cell Metab*. **18**(3): 392 – 402.

Liu Q., Hollopeter G., Jorgensen E.M. 2009. Graded synaptic transmission at the *Caenorhabditis elegans* neuromuscular junction. *Proc. Natl. Acad. Sci. U.S.A.* **106**: 10823–10828.

Maruyama I.N., Brenner S. 1991 A phorbol ester/diacylglycerol-binding protein encoded by the *unc-13* gene of *Caenorhabditis elegans*. *Proc Natl Acad Sci USA* **88**:5729–5733.

McIntire S.L., Reimer R.J., Schuske K., Edwards R.H., Jorgensen E.M. 1997. Identification and characterization of the vesicular GABA transporter. *Nature,* **389**: 870–876.

McIntire S.L., Jorgensen E.M., Kaplan J.M., Horvitz H.R. 1993. The GABAergic nervous system of Caenorhabditis elegans. *Nature*, **36:** 337-341.

Mellem J.E., Brockie P.J., Zheng Y., Madsen D.M. Maricq, A.V. 2002. Decoding of polymodal sensory stimuli by postsynaptic glutamate receptors in *C. elegans*. *Neuron,* **36**: 933–944.

Meloni I., Sachidanadan D., Thum A.S., Kittel R.J., Murawski C. 2020. Controlling the behaviour of *Drosophila melanogaster* via smartphone optogenetics. *Sci Rep***, 10**: 17614.

Miller K.G., Alfonso A., Nguyen M., Crowell J.A., Johnson C.D., Rand J.B. 1996. A genetic selection for *Caenorhabditis elegans* synaptic transmission mutants. *Proc Natl Acad Sci USA,* **93**:12593–12598.

Milward K., Busch K.E., Murphy R.J., de Bono M., Olofsson, B. 2011. Neuronal and molecular substrates for optimal foraging in *Caenorhabditis elegans*. *Proc. Natl. Acad. Sci. U.S.A.* **108**: 20672–20677.

Moser B.K., G.R. 1992. Stevens Homogeneity of Variance in the Two Sample Means Test. *The American Statistician, **46***(1):19-22.

Mulcahy B., Holden-Dye L., O'Connor V. 2013. Pharmacological assays reveal age-related changes in synaptic transmission at the *Caenorhabditis elegans* neuromuscular junction that are modified by reduced insulin signalling. *Journal of Experimental Biology*, **216:** 492-501.

Murakami H., Bessinger K., Hellmann J., Murakami S. 2005. Aging-dependent and -independent modulation of associative learning behavior by insulin/insulin-like growth factor-1 signal in Caenorhabditis elegans. *The Journal of neuroscience: the official journal of the Society for Neuroscience.* **25**:10894–10904.

Nagel G., Brauner M., Liewald J.F., Adeishvili N., Bamberg E., Gottschalk, A. 2005. Light activation of channelrhodopsin-2 in excitable cells of *Caenorhabditis elegans* triggers rapid behavioral responses. *Curr. Biol.* **15**: 2279–2284.

Nagel G., Szellas T., Huhn W., Kateriya S., Adeishvili N., Berthold P., Ollig D., Hegemann P., Bamberg, E. 2003. Channelrhodopsin-2, a directly light-gated cation-selective membrane channel. *Proc. Natl. Acad. Sci. U.S.A.* **100**: 13940–13945.

Narayan A., Laurent G., Sternberg P.W. 2011. Transfer characteristics of a thermosensory synapse in *Caenorhabditis elegans*. *Proc. Natl. Acad. Sci. U.S.A.* **108**: 9667–9672.

Nonet M.L., Grundahl K., Meyer B.J., Rand J.B. 1993. Synaptic function is impaired but not eliminated in *C. elegans* mutants lacking synaptotagmin. *Cell,* **73**:1291–1305.

Nonet M.L., Saifee O., Zhao H., Rand J.B., Wei L. 1998. Synaptic transmission deficits in *Caenorhabditis elegans* synaptobrevin mutants. *J Neurosci,* **18**:70–80.

Nussbaum-Krammer C.I., Neto M.F., Brielmann R.M., Pedersen J.S., Morimoto R.I. 2015. Investigating the spreading and toxicity of prion-like protein using the metazoan model organism C. elegans. *J Vis Exp.* **95**: 52321.

O'Hagan R., Chalfie M., Goodman M.B. 2005. The MEC-4 DEG/ENaC channel of *Caenorhabditis elegans* touch receptor neurons transduce mechanical signals. *Nat. Neurosci*. **8**, 43–50.

Oh C-H., Shim J-I., Shin D-S. 2019. Current- and temperature-dependent efficiency droops in InGaN-based blue and AlGaInP-based red light-emitting diodes. *Jpn. J. Appl. Phys.* **58**: SCCC08.

Pan C.L., Peng C.Y., Chen C.H., McIntire S. 2011. Genetic analysis of age-dependent defects of the Caenorhabditis elegans touch receptor neurons. *Proc. Natl. Acad. Sci. U.S.A*. **108**:9274–9279.

Park J., Lee C.C. 2005. An electrical model with junction temperature for light-emitting diodes and the impact on conversion efficiency. *IEEE Electron Device Letters,* **26**: 5.

Perni, M., Challa P.K., Kirkegaard J.B., Limbocker R., Koopman M., Hardenberg M.C., Sormanni P., Muller T., Saar K.L., Roode L.W.Y., Habchi J., Vecchi G., Fernando N., Casford S., Nollen E.A.A., Vendruscolo M., Dobson C.M., Knowles T.P.J. 2018. Massively parallel *C. elegans* tracking provides multi-dimensional fingerprints for phenotypic discovery. *Journal of Neuroscience Methods*, **306**: 57-67.

Piggott B.J., Liu J., Feng Z., Wescott S.A., Xu X.Z.S. 2011. The neural circuits and synaptic mechanisms underlying motor initiation in *C. elegans*. *Cell,* **147**: 922–933.

Pokala N., Glater E. E. 2018. Using optogenetics to understand neuronal mechanisms underlying behavior in *C. elegans. J. Undergrad. Neurosci. Educ.* **16**: A152–A158.

Pulver S.R., Hornstein N.J., Land B.L., Johnson B.R. 2011. Optogenetics in the teaching laboratory: using channelrhodopsin-2 to study the neural basis of behavior and synaptic physiology in *Drosophila*. *Adv Physiol Educ*, **35**:82–91.

Pulver S.R., Stanislav L., Pashkovski L., Hornstein N.J., Garrity P.A. Griffith L.C. 2009. Temporal dynamics of neuronal activation by channelrhodopsin-2 and TRPA1 determine behavioral output in *Drosophila* larvae. *J Neurophysiol*, **101**(6): 3075-3088.

Qiu Z., Tu L., Huang L., Zhu T., Nock V., Yu E., Liu X., Wang W. 2015. An integrated platform enabling optogenetic illumination of *Caenorhabditis elegans*neurons and muscular force measurement in microstructured environments. *Biomicrofluidics*, **9**: 014123.

Rabinowitch I., Laurent P., Zhao B., Walker D., Beets I., Schoofs L., Bai J., Schafer W. R., Treinin M. 2016a. Neuropeptide-driven cross-modal plasticity following sensory loss in *Caenorhabditis elegans*. *PLoS Biol.* **14**: e1002348.

Rabinowitch I., Treinin M., Bai J. 2016b. Artificial optogenetic TRN stimulation of *C. elegans*. *Bio-Protocol,* **6**(20): e1966.

Ramot D., Johnson B.E., Berry T.L., Carnell L., Goodman M.B. 2008b. The parallel worm tracker: a platform for measuring average speed and drug-induced paralysis in nematodes. *PLoS ONE,* **3**: e2208.

Ramot D., MacInnis B.L., Goodman, M.B. 2008a. Bidirectional temperature-sensing by a single thermosensory neuron in *C. elegans*. *Nat. Neurosci.* **11**: 908–915.

Rand J.B., Russell R.L. 1984. Choline acetyltransferase-deficient mutants of the nematode *Caenorhabditis elegans*. *Genetics,* **106**:227–248.

Rand J.B., Russell R.L. 1985. Molecular basis of drug-resistance mutations in *C. elegans*. *Psychopharmacol Bull,* **21**:623–630.

Restif C., Ibanez-Ventoseo C., Vora M.M., Guo S., Metaxas D., Driscoll M. 2014. CeleST: computer vision software for quantitative analysis of C. elegans swim behavior reveals novel features of locomotion. *PLoS Computational Biology*, **17**: e1003702.

Richmond J.E. 2006. Electrophysiological recordings from the neuromuscular junction of *C. elegans*. *WormBook*, 1-8.

Richmond J.E. and Jorgensen E.M. 1999a. One GABA and two acetylcholine receptors function at the *C. elegans* neuromuscular junction. *Nat. Neurosci*, **2**: 791-797.

Richmond J.E., Davis W.S., Jorgensen E.M. 1999b. UNC-13 is required for synaptic vesicle fusion in *C. elegans*. *Nat. Neurosci* **2:** 959–964.

Richmond, J. 2009. Dissecting and recording from the *C. elegans* neuromuscular junction. *J. Vis. Exp*. **24**: 1165.

Sassa T., Harada S., Ogawa H., Rand J.B., Maruyama I.N., Hosono R. 1999. Regulation of the UNC-18-*Caenorhabditis elgegans* syntaxis complex by UNC-13. *Journal of Neuroscience,* **19**(12): 4772-4777.

Sawin E.R., Ranganathan R., Horvitz H.R. 2000. C. elegans locomotory rate is modulated by the environment through a dopaminergic pathway and by experience through a serotonergic pathway. *Neuron*, **26**(3): 619-631.

Schmitt C., Schultheis C., Pokala N., Husson S.J., Liewald J.F., Bargmann C.I., Gottschalk A. 2012. Specific Expression of Channelrhodopsin-2 in Single Neurons of Caenorhabditis elegans. *PLOS ONE* **8**(2): e43164.

Schroll C., Riemensperger T., Bucher D., Ehmer J., Voller T., Erbguth K., Gerber B., Hendel T., Nagel G., Buchner E., Fiala A. 2006. Light-induced activation of distinct modulatory neurons triggers appetitive or aversive learning in Drosophila larvae. *Curr. Biol.* **16**: 1741–1747.

Schultheis C., Liewald J.F., Bamberg E., Nagel G., Gottschalk A. 2011a. Optogenetic long-term manipulation of behavior and animal development. *PLoS ONE,* **6**: e18766.

Schultheis C., Brauner M., Liewald, J.F., Gottschalk A. 2011b. Optogenetic analysis of GABAB receptor signaling in *Caenorhabditis elegans* motor neurons. *J. Neurophysiol*. **106**: 817–827.

Schuske K., Beg A.A., Jorgensen E.M. 2004. The GABA nervous system in *C. elegans*. *Trends in Neuroscience*, **27**(1): 407-414.

Schuske K.R., Richmond J.E., Matthies D.S., Davis W.S., Runz S., Rube D.A., van der Bloek A.M., Jorgensen E.M. 2003. Endophilin is required for synaptic vesicle endocytosis by localizing synaptojanin. *Neuron*, **40**: 749–762.

Stirman J. N., Brauner M., Gottschalk A., Lu H. 2010. High-throughput study of synaptic transmission at the neuromuscular junction enabled by optogenetics and microfluidics. *J. Neurosci. Methods,* **191**: 90–93.

Stirman J.N., Crane M.M., Husson S.J., Wabnig S., Schultheis C., Gottschalk A., Lu H. 2011. Real-time multimodel optical control of neurons and muscles in freely behaving *Caenorhandities elegans*. *Nat Methods.* **8**(2): 153-158.

Swierczek N.A., Giles A.C., Rankin C.H., Kerr R.A. 2011. High-throughput behavioural analysis in *C. elegans*. *Nat. Methods.* **8**(7): 592-598.

Tank E.M., Rodgers K.E., Kenyon C. 2011. Spontaneous age-related neurite branching in Caenorhabditis elegans. *The Journal of neuroscience: the official journal of the Society for Neuroscience*. **31**:9279–9288.

Tien C.W., Yu B., Huang M., Stepien K.P., Sugita K., Xie X., Han L., Monnier P.P., Zhen M., Rizo J., Gao S., Sugita A. 2020. Open syntaxin overcomes exocytosis defects of diverse mutants in *C. elegans*. *Nat Commun* **11**: 5516.

Toth M.L., Melentijevic I., Shah L., Bhatia A., Lu K., Talwar A., Naji H., Ibanez-Ventoso C., Ghose P., Jevince A., Xue J., Herndon L.A., Bhanot G., Rongo C., Hall D.H., Driscoll M. 2012. Neurite sprouting and synapse deterioration in the aging Caenorhabditis elegans nervous system. *The Journal of neuroscience: the official journal of the Society for Neuroscience.* **32**:8778–8790.

Tsibidis G.D., Tavernarakis N. 2007. *Nemo:* a computational tool for analysing nematode locomotion. *BMC Neuroscience,* **8**: 86.

Wang S.J., Wang Z-W. 2013. Track-A-Worm, an open-source system for quantitative assessment of *C. elegans* locomotory and bending behavior. *PLoS ONE.* **8**(7): e69653.

Waschuk S.A., Bezerra A.G., Shi L., Brown L.S. 2005. Leptosphaeria rhodopsin: bacteriorhodopsin-like proton pump from a eukaryote. *Proc Natl Acad Sci USA,* **102**: 6879-6883.

Weissenberger S., Schultheis C., Liewald J. F., Erbguth K., Nagel G., Gottschalk A. 2011. PACα—An optogenetic tool for in vivo manipulation of cellular cAMP levels, neurotransmitter release, and behavior in *Caenorhabditis elegans J. Neurochem.* **116**: 616–625.

White J.G., Southgate E., Thomson J.N., Brenner S. 1986. The structure of the nervous system of the nematode Caenorhabditis elegans. *Phil. Trans. R. Soc. Lond. B.* **314**: 1-340.

Yang X., Sun B., Wang Z., Qian C., Ren Y., Yang D., Feng Q. 2018. An Alternative Lifetime Model for White Light Emitting Diodes under Thermal–Electrical Stresses. *Materials (Basel, Switzerland)*, **11**(5): 817.

Zhang F., Wang L.P., Brauner M., Liewald J.F., Kay K., Watzke N., Wood P.G., Bamberg E., Nagel G., Gottschalk A., Deisseroth K. 2007. Multimodal fast optical interrogation of neural circuitry. *Nature,* **446**: 633–639.

1195 # Figure legends

1196 **Figure 1: Channelrhodopsin-2 is a light-sensitive cation channel**

1197 **A)** Channelrhodopsin-2 (ChR2) is rapidly opened by stimulation with blue (440-460 nm) light in an essentially
1198 nondesensitizing manner. ChR2 is permeable by multiple cations like Na^+ and Ca^{2+} and enables strong and rapid
1199 membrane depolarization of the cell it is expressed in. **B)** Multiple ChR2-expressing C. elegans strains exist,
1200 including but not limited to expressing in muscle cells (*myo-3*), cholinergic neurons (*unc-17*) and GABAergic
1201 neurons (*unc-47*). **C)** The change in body length is often used as a read-out of ChR2 activation (see B).

1202
1203
1204 **Figure 2: Building the OptoArm only requires basic knowledge of electronics and thermal management**

1205 **A)** The optimal electronic circuitry of the OptoArm. Inset: the variant of the circuitry used in this paper to test and
1206 validate the system. The color codes refer to the wires of the LED-driver that is used in this paper. **B)** The essential
1207 components required to build the electronic circuitry of the OptoArm: 1. Luxeon Rebel LED, 2. Thermal adhesives,
1208 3. Heatsink, 4. Wire harness with potentiometer, 5. DC-plug, 6. ON/OFF button, 7. LED driver, 8. lens with case,
1209 9. Several lenses, 10. and 11. Lens holder. **C)** The steps required to construct the OptoArm, detailed instructions
1210 per picture can be found in Table 2. *STEP 1:* connecting the solderless DC-plug to the connecting wire harness.
1211 *STEP 2*: mounting the LED on a heatsink and soldering the connecting wire harness to the LED cathode and anode.
1212 *STEP 3*: Connecting the ON/OF switch to the LED driver and connecting the driver to the wire harness. Note, the
1213 pictures show a serial set-up, and not the recommend parallel wiring (see 2A, main). *STEP 4*: mounting the
1214 electronic circuitry to a standard flask clamp to finish the OptoArm. By placing the OptoArm in either a **D)** fine-
1215 tuner or a **E)** general lab standard, the system can be used for different applications. **F)** The different thermal
1216 resistances ($R\theta$) in the heat flow between the LED junction, temperature test point and bottom of the LED
1217 assembly.

1218
1219 **Figure 3: The OptoArm provides the light intensity and stability required for optogenetic experiments**

1220 **A)** The different lenses used for testing. **B)** A schematic outlining the tested parameters with the three different
1221 lenses. **C)** Raster showing the *x,y* coordinates used to measure the intensity of the LED. **D)** The different integrated
1222 intensity profiles of the LED with and without lenses. The histograms show the zoomed-in distribution of intensity-
1223 readings between a minimum and maximum intensity with a specified bin width. Red lines show the average
1224 intensity. **E)** Smoothened histograms of D that show the increase in intensity when using different lenses with the
1225 OptoArm. **F)** Schematic showing the method to assess the stability of intensity over time. **G)** Distributions of

1226 intensity readings at the different time-point without a lens **H)** and with a 10º lens. All readings were performed
1227 at 448nm.
1228
1229 **Figure 4: The OptoArm fulfills all technical criteria in different experimental set-ups**
1230 **A)** The OptoArm set-up used with a standard dissection microscope. **B)** In experimental set-ups, the OptoArm is
1231 used with a specific angle (43 °), thereby deviating from perpendicular illumination. **C)** The different illumination
1232 profiles for the different lenses upon and illumination with the specified angle of incidence. **D)** The different
1233 integrated intensity profiles for C. The histograms show the distribution of intensity-readings between a minimum
1234 and maximum intensity with a specified bin width. Red lines show the average intensity. **E)** Schematic showing
1235 the different visible microscopic areas (of the used microscope) when using different magnifications. The areas
1236 are on scale and can be directly compared to the intensity maps shown in D. 1.0x corresponds to a total
1237 magnification of 15x, and 4.0 to a total of 60x. The dotted red line represents the area in D with an intensity of
1238 >1.6 mW/mm^2. **F)** The OptoArm set-up with the WF-NTP. **G)** The different integrated intensity profiles of the
1239 LED with the 21º lens, at different working distances with a fixed angle of incidence of 43º. Profiles were generated
1240 in the set-up with the WF-NTP. Circles represent the outline of a 3-cm NGM plate. **H)** Histograms of intensity-
1241 readings of the microscope-light (gaussian) and WF-NTP back-light (flat-field). Red lines show the average
1242 intensity. All readings were performed at 448nm. **I)** Thrashing frequency of D1 worms, expressing ChR2 under
1243 the *unc-17* (acetylcholine) or *unc-47* (GABA) promotor, recorded with the WF-NTP, grown with or without ATR.
1244 There is no significant effect of the WF-NTP light on this behavior, $n = 15$, two-tailed unpaired Student's t test
1245 (all: n.s.). **J)** Body length of D1 worms recorded with the WF-NTP, grown with or without ATR. Body length was
1246 normalized by the mean the of the paired ATR- condition. There is no significant effect of the WF-NTP light on
1247 this behavior, $n = 15$, two-tailed unpaired Student's t test (all: n.s.). For **I)** and **J**) there was no photostimulation
1248 with the OptoArm.
1249
1250
1251 **Figure 5: The OptoArm allows manual intensity-adjustments, which modulate biological readouts.**
1252 **A)** To record worms in an inexpensive way, we used a Carson smartphone adapter to place and orient a cellphone
1253 camera to a microscope. A blue-light filter was placed between the ocular and sample to avoid interference of the
1254 blue light with recording. **B)** Schematic of the experimental outline: *a priori* determined intensities (0.2, 0.4, 0.8.,
1255 1.2., 1.6 and 1.8 mW/mm^2) were set by adjusting the resistance of the potentiometer. At the different intensities
1256 the Δ body length was measured**. C)** The histograms show the distribution of intensity-readings at *a priori* specified

1257 intensities. Red lines show the average intensity. **D)** Smoothened histograms of C that show the increase in
1258 intensity when adjusting the resistance of the potentiometer. **E)** Pictures of a D1 worms (*myo-3p::ChR2::YFP)*
1259 just before and during illumination with 1.6 mW/mm^2 blue light. Scale bar: 200 um. **F)** The different body lengths
1260 (normalized to length before illumination) at different intensities of illumination with the OptoArm. Calculated
1261 via a midline-approach, n = 10.
1262
1263 **Figure 6: A semi-automatic perimeter-approach is a reliable way of assessing changes in body length during**
1264 **and after optogenetic stimulation.**
1265 **A)** Schematic outline of image-processing in ImageJ to follow body-length changes over time in a semi-automatic
1266 way. **B)** Raw readings of body length (perimeter in pixels) of a worm expressing ChR2 in cholinergic neurons
1267 (*unc-17p::ChR2::YFP)* plotted against time in milliseconds, the graph represents n = 1. **C)** The change in body
1268 lengths (normalized to length before illumination) of multiple worms, *n = 10*, when using a perimeter approach to
1269 estimate the worm length. Δ body length equals the change in length before illumination and during illumination.
1270 **D)** Schematic of a worm with the midline and perimeter highlighted. **E)** The relationship between the midline of
1271 the worm and the perimeter. *n = 70* (35 still images of worms at light ON and 35 worms at light OFF). The
1272 spearman correlation was calculated (p<0.001).
1273
1274 **Figure 7: Mutations in the cholinergic or GABAergic system affect Δ body length after optogenetic**
1275 **stimulation with the OptoArm.**
1276 **A)** A schematic showing the different mutant used to verify previously established results. **B)** Schematic of the
1277 experimental outline: the change in body length was measured after blue light stimulation with an intensity of 1.6
1278 mW/mm^2. **C)** Kinetics of optogenetic stimulation in mean ±SEM body length of control worms and *unc-26(s1710*)
1279 and *unc-47(e307)* mutants expressing ChR2 in cholinergic neurons, *n = 9-10*. A perimeter-approach was used. **D)**
1280 Quantification of mean ±SEM normalized body length of control D1 worms and *unc-26(s1710)* and *unc-47(e307)*
1281 mutants expressing ChR2 in cholinergic neurons. Two-way ANOVA (Interaction, ATR, Genotype: p<0.001) with
1282 post-hoc Dunnett, *n = 11-15* for ATR+ and *n = 5-6* for ATR-. A midline-approach was used. **E)** Kinetics of
1283 optogenetic stimulation in mean ±SEM normalized body length of control worms and *unc-26(s1710)* and *unc-*
1284 *47(e307)* mutants expressing ChR2 in GABAergic neurons, *n = 9-11.* A perimeter-approach was used. **F)**
1285 Quantification of mean ±SEM normalized body length of control worms and *unc-26(s1710)* and *unc-47(e307)*
1286 mutants expressing ChR2 in GABAergic neurons. Two-way ANOVA (Interaction, ATR, Genotype: p<0.001) with

1287 post-hoc Dunnett, *n = 10-15* for ATR+ and *n = 5-6* for ATR-. A midline-approach was used**. G)** Long-term
1288 photostimulation of control worms, unc-26(s1710) and unc-47(e307) mutants expressing ChR2 in cholinergic
1289 neurons. Two-way repeated ANOVA with Geisser-Greenhouse correction (time, genotype, time x genotype and
1290 individual worms: $p<0.001$) and post-hoc Dunnett, *n = 10*. A midline-approach was used. Blue bars represent
1291 'light ON'. Acetylcholine: *zxIs6 (Punc-17::ChR2::YFP), zxIs3 (Punc-47::ChR2::YFP).* All experiments were
1292 replicated three times, one representative experiment is shown. *: $p \leq 0.05$, **: $p \leq 0.01$, ***: $p \leq 0.001$. Error
1293 bars represent S.E.M.
1294
1295 **Figure 8: Population characteristics acquired with the WF-NTP are potential readouts of optogenetic**
1296 **stimulation with the OptoArm.**
1297 **A)** Schematic of experimental outline. D4 worms were assessed in liquid with the OptoArm being OFF and ON
1298 and population characteristics (bending frequency and eccentricity) were analyzed with the WF-NTP software. **B)**
1299 Change in bends per 30 seconds when light is ON of worms grown with or without ATR. The percentual decline
1300 in thrashing capacity is annotated in the graph, *n = 15.* For acetylcholine: Mann Whitney U test $p<0.001$, GABA:
1301 two-tailed unpaired Student's t test: $p<0.001$. **C)** Binned effect of blue-light on swimming behavior of transgenic
1302 worms grown with or without ATR, *n = 10*. Two-way ANOVA (time, genotype, interaction: $p<0.001$) with post-
1303 hoc Sidak's. **D)** Change in bends per 10 seconds after optogenetic stimulation. Acetylcholine: only the last 10
1304 seconds of 30s-illumination is used, GABA: only the first 10 seconds are used. *n = 15.* For acetylcholine: Mann
1305 Whitney U test $p<0.001$, GABA: two-tailed unpaired Student's t test: $p<0.001$. **E)** Effect of blue-light on
1306 eccentricity of worms grown with or **F)** without ATR. *n = 20 – 40,* Mann-Whitney U tests Acetylcholine + ATR:
1307 0-10s: not significant, 10-20s: $p=0.0192$, 20-30s: $p=0.0033$, for 0-30s: $p = 0.0427$. Acetylcholine – ATR, and both
1308 GABA conditions: n.s. **G)** The body length of worms expressing ChR2 under the *unc-17* promoter after blue-light
1309 stimulation, *n = 15,* two-tailed unpaired Student's t test: n.s. Blue bars represent 'light ON'. Acetylcholine: *zxIs6*
1310 *(Punc-17::ChR2::YFP), zxIs3 (Punc-47::ChR2::YFP).* All experiments were replicated three times, one
1311 representative experiment is shown. *: $p \leq 0.05$, **: $p \leq 0.01$, ***: $p \leq 0.001$.
1312
1313 **Figure 9: Cholinergic neuronal ageing correlates best with the decline in motility.**
1314 **A)** Schematic showing the experimental outline. The Δ body length was determined for strains expressing ChR2
1315 in muscle, cholinergic neurons and GABAergic neurons at several time-intervals. At the same time the movement
1316 capacity, represented as bends per 30 seconds in liquid, was also measured. **B)** The decline in thrashing capacity

in liquid of worms expressing ChR2 in cholinergic of GABAergic neurons. *n = 15*, two-way ANOVA (Age: $p<0.001$, interaction and neuron type: n.s.). The experiment was triplicated, one representative experiment is shown. **C)** The normalized Δ body length (elongation for GABA, contraction for muscle and cholinergic neurons) at different ages as measured by the midline-approach. Every point represents the mean of an experiment with > 10 biological replicates each. Fitted lines represents a general linear model with 2nd order polynomial fit. All points within one experiment were normalized by the intra-experimental average at D1 within each strain. **D)** The average decline in thrashing ability over time. Every point represents the mean of an experiment with > 20 biological replicates each. All points were normalized by the inter-experimental average at D1 within each strain. This sets the average bends per 30 seconds to exactly 1.0 at D1. Fitted lines represents a general linear model with 2nd order polynomial fit. **E)** The correlation between the Δ body length and Δ movement capacity (normalized to the changes and capacity at D1 intra-experimentally). Fitted lines represent simple linear regression without restrictions (both slopes deviate significantly from zero: $p<0.001$). The black line corresponds to a relation of $x = y$, in which the decline in movement is equal to the decline in Δ body length. **F)** The Δ eccentricity (eccentricity before illumination minus eccentricity during illumination) at different ages after optogenetic stimulation. Each individual point represents the mean of $n > 15$ worms. Student's t test: n.s. All experiments were replicated three times. The transparent zones around the fitted lines represents the confidence interval (95%). *: $p \leq 0.05$, **: $p \leq 0.01$, ***: $p \leq 0.001$.

Figure 10: Automation of the OptoArm allows fine-adjustment of light pulse-width and intensity.

A) The electronic circuitry of the OptoArm under the control of a micro-controller (an Arduino uno in this paper). **B)** By using a pulse-width modulator output pin of Arduino the pulse-width (I, II), time-intervals (III) and intensity (IV) op the OptoArm can be easily regulated. **C)** By using an LCD-shield on top of an Arduino uno, all parameters can be adjusted in live-modus without the intervention of a computer. There are 5 buttons that can be used to go UP and DOWN in the different programs to select parameters and to adjust them by pressing LEFT or RIGHT. All changes can be confirmed with the SELECT button (see Table 3). **D)** The different programs of the automated OptoArm. Program 1 (I) allows testing the system and manually turning the LED ON and OFF (II). Here, the intensity of the system can be changed as well. Program 2 (III) can be used to give single-timed pulses of light (IV). Program 3 (V) can be used to give trains of single-time pulses. One can adjust both the pulse-time (IV), the waiting time and the number of cycles (IV). **E)** The software provides a clear overview of the steps that are

performed. When a run is started and then finishes, the user can use the option ‘Rerun’ to execute the same program without having to adjust the parameters again.

Tables

TABLE 1: Different variants of the OptoArm, their requirements and costs

	Minimal requirements OptoArm[a] (Figure 2)	**Minimal requirements OptoArm with low-cost stand[a,b] (Figure 2)**	**Automated OptoArm with low-cost stand[a] (Figure 10)**	**Additional improvements or available changes[a, d]**
Electronics	>Royal-Blue (448nm) Rebel LED >700 mA externally dimmable BuckPuck DC driver >Connecting wire with adjustable potentiometer of 5 kΩ >Latching pressure switch (ON/OFF switch) >DC contra plug >9V_{DC} – Adapter	**All the previously mentioned components**	**All the previously mentioned components except:** >Connecting wire with adjustable potentiometer of 5 kΩ **Plus:** > Arduino uno (or clone) > Capacitor (0.1 uf) > Adafruit LCD-shield	**Yellow LED for NpHR/Halo/Mac[e]:** e.g Lime (567nm) Rebel LED on a SinkPAD-II 20mm Star Base - 368 lm @ 700mA COST: $11 **Tri-star LED for higher intensity[e]:** Royal-Blue (448nm) Rebel LED on a SinkPAD-II 20mm Tri-Star Base - 3090 mW @ 700mA. COSTS: $14
Heat management	>Heatsink 5.2 °C/W >Pre-cut thermal adhesive tape	**All the previously mentioned components**	**All the previously mentioned components**	-
Optics	>Khatod 10° lens >Fraen 21° lens >Khatod 40° lens	**All the previously mentioned components**	**All the previously mentioned components**	-
Mounting	>Lens-holder >Three-pronged clamp	**All the previously mentioned components AND:** > Stand rod > Double boss-head > Retort stand base, tripod	**All the previously mentioned components**	**Comar fine-tuner stand[f]:** Basic carrier, pinion stage, post-holder, rod, self-manufactured base. COSTS: ~ $ 280 **Cross-clamp to fixate DC-plug on arm[g]:** COSTS: ~ $12
Average costs	**~ $ 65**	**~ $ 90**	**~ $ 128[c]** **(Arduino clone: $ 116)**	

[a] For components originally listed in euros, we calculated the dollar prize with the current exchange rate in mind. All prices are excluding soldering material and standard materials such as extra wires and shrink tubing. Also, standard worm equipment is not taken into account (e.g. microscopes and worm trackers). [b] The low-cost stand provides a way to work with the WF-NTP and a microscope set-up and is therefore the most flexible. [c] The price is based on an original Arduino uno R3. Clones tend to be much cheaper, but identical in the board lay-out. [d] The components are not essential, but potential substitutes or additions. [e] When a Tri-Star LED or any other LED is used, we highly recommend to re-evaluate the thermal management. The heatsink of the OptoArm was specifically selected based on the specification of a single royal-blue LED. [f] The Comar fine-tuner stand is a more expensive stand, but allows fine-adjustments of height due to the pinion stage. All the specifications can be found in the method section. [g] We did use the cross-clamp to organize the OptoArm and fixate the DC contra plug, see Figure 2C.

TABLE 2: Instructions for building the OptoArm (see Figure 2C)

Steps	Goal	Instructions[a]	Critical notes
Step 1	Connecting power	In order to connect a DC-adapter to the optogenetics system, we use a soldering-free DC-plug. The black and red wires of the connecting wire harness (I) should be attached to the DC-plug (II, III). Note that the used wire harness has already a 5 kΩ potentiometer pre-installed. When using a different system, make sure to manually add a potentiometer parallel to the switch between the yellow (REF) and grey (CTRL) wires.	Determine the center and barrel polarity of the system to ensure appropriate wiring (with a multimeter)
Step 2	Connecting LED and thermal management	For appropriate thermal management use a heatsink that fulfils the criteria of the system (see *thermal management*, box 1). Clean the heatsink with ethanol before adding a pre-cut thermal adhesive (I). Remove the top-layer of the thermal adhesive and place the LED on top of it (II). Apply firm pressure for at least 30 seconds with an assembly press that's included with the single rebel led (III). Solder the blue and white wires of the connecting wire harness to the cathode and anode of the LED respectively. Then, cut some pre-cut thermal adhesive in the shape of the lens-holder and attach the lens-holder via the tape to the heatsink (IV). Finally, by loosening the screw of the lens-holder, lenses can be added to or removed from the system (V).	It is important to solder when the LED is already on the heatsink to ensure heat-dissipation and circumvent overheating of the LED
Step 3	Connecting swtich and LED driver	Add the ON/OFF switch (I) and LED driver (II) to the system (III, IV). The driver can be connected to the wire harness by soldering male pin connectors to the wires of the LED-driver and clicking them in the connecting wire harness. Note, that the pictures (Figure 2C) show the serial set-up used in the paper, in which the red-wire coming from the DC-plug is connected with the ON/OFF switch before connecting to the LED-driver. We recommend to place the switch in parallel to the potentiometer between the yellow and grey wires (See Figure 2A).	The placement of the ON/OFF switch between the CTRL and REF pins, in parallel with the potentiometer provides the best management of inrush power and spikes to the LED.
Step 4	Mounting on the arm: the final OptoArm	Add the whole circuitry to a standard flask clamp (I). Use a cross clamp to fixate the DC-plug on the arm (II, III). By placing the OptoArm in either a fine-tuner or a general lab standard, the system can be used for different applications.	-

[a] The different steps and roman numerals refer to those used in Figure 2C.

TABLE 3: Arduino controls and button functions

Display screen	Controls	Function	Fig. 10
Main	UP/DOWN	Scroll through program options	D: I,III,V
	SELECT	Confirm selection	
Program 1 settings	UP/DOWN	Set intensity	D: II
	LEFT/RIGHT	Switch between ON/OFF/MAIN	
	SELECT	Confirm return to main menu	
Program 2/3 settings	LEFT/RIGHT	Set parameter value	D: IV, VI
	SELECT	Confirm settings, skip to next display	
Program 3 settings	UP/DOWN	Switch between parameters	D: VI
Start run	LEFT/RIGHT	Switch between yes/no	E: I
	SELECT	Confirm selection	
Finish	LEFT/RIGHT	Switch between rerun/return to main	E: II
	SELECT	Confirm selection	

Boxes

BOX 1: Calculating the required thermal properties of a heat sink

Using the following thermal model (eq. 1, Lin et al., 2011, Figure 2F) and calculating or estimating all the individual parameters (eq. 2-4) the required thermal properties of a heat sink can be calculated.

$$R\theta_{J-Ref} = \frac{\Delta T_{J-Ref}}{P_D} \quad (1)$$

Where:

$R\theta_{J-Ref}$ = Thermal resistance (ºC/W) from the LED-junction to a reference point (2)

= $R\theta_{Junction-Thermalpad} + R\theta_{Thermalpad-Solderpad} + R\theta_{Solderpad-Adhesives} + R\theta_{Adhesive-heatsink}$

ΔT_{J-Ref} = (T_J, junction temperature) – (T_{Ref}, reference point temperature, ºC) (3)

PD = Power dissipation (W) (4)

= LED forward current (I_f) * LED forward voltage (V_f)

Typically, the maximal junction temperature can be found in the datasheet for the LED. For a Royal blue Luxeon Rebel LED on a SinkPAD-II, that is used in this paper, the listed temperature is 150 ºC. Ideally, the operating temperature should be well below that limit, as even reaching this temperature for a fraction of time could influence the properties of the LED (Yang et al., 2018; Oh et al., 2019; Fu et al., 2018; Kim, et al., 2016). Therefore, we decided to set the maximum junction temperature to 100 ºC. Next, the power dissipation of the same LED can be calculated by multiplying the forward voltage rating of the LED with the drive current in Amperes (eq. 4). Since we use a fixed 700 mA LED-driver and know the maximal voltage drop of the LED (3.5V), P_d is easily calculated (eq. 4). Finally, the maximal thermal resistance should be calculated by taking in the maximum working ambient temperature into account, which was determined to be 25 ºC (20 ºC room temperature + 5 ºC margin, eq. 3). Importantly, note that our set-up is located in a climate-controlled room. If this is not the case, a wider margin for temperature fluctuations and higher maximum temperature based on local environmental conditions should be considered. Rewriting eq. 1 and calculating $R\theta$ gives (eq. 5):

$$R\theta_{J-Ref} = \frac{\Delta T_{J-Ref}}{P_D} = \frac{\Delta T_{J-Ref}}{If\ x\ Vf} = \frac{100-25}{0.7 \times 3.5} = 30.6\ ºC/W \quad (5)$$

This means that the total thermal resistance of the system can be maximally 30.6 ºC/W (eq. 2) when one aims for junction temperatures that are maximally 100 ºC. In order to see what that means for the required heatsink, all the known thermal resistances (Figure 2F) can be collected from the datasheets of the LED (junction to thermal pad: 6.0 ºC/W and thermal pad to solder pad: 0.7 ºC/W) and used adhesives (4.5 ºC/W). Rewriting eq 2. gives (eq. 6):

$$R\theta_{Adhesive-Heatsink} = R\theta_{J-Ref} - R\theta_{Junction-Thermalpad} - R\theta_{Thermalpad-Solderpad} - R\theta_{Solderpad-Adhesives} \quad (6)$$

$$= 30.6 - 6.0 - 0.7 - 4.5$$

$$= 19.4 \text{ ºC/W}$$

Theoretically, a heatsink in this set-up can have a maximal thermal resistance of 19.4 ºC/W and any heatsink with lower resistance than that can be used. We used a finned heatsink with thermal resistance of 5.2 ºC/W to keep the set-up compact and still achieve sufficient cooling. Next, we continued with an empirical approach to verify whether appropriate heat dissipation could be obtained with this set-up. Therefore, we measured the actual junction temperature and the voltage drop of the LED mounted to the OptoArm (Figure 2D). With a Fluke TM80 module and associated test probe, we measured the temperature at the specified test-location (Figure 2F) of the LED for about 1 minute until the temperature stabilized. At the same temperature, we also determined the actual voltage drop of the LED. We measured a temperature of 55.68 $\pm$ 0.76 ºC (*n = 10*) and a forward drop of 2.972 $\pm$ 0.004 V (*n = 5*). By using eq. 7, the actual junction temperature can be derived:

$$T_{Junction} = T_{testpoint} + \left(R\theta_{Junction-Thermalpad} + R\theta_{Thermalpad-testpoint}\right) \times (V_f \times I_f) \quad (7)$$

$$= 55.68 \text{ °C} + (6.0 \text{ °C/W} + 0.5 \text{ °C/W}) \times (2.972\, V \times 0.7\, A) = 69.2 \text{ °C}$$

With an estimated junction temperature of 69.2 ºC, the system fulfills our criteria for a system with appropriate thermal cooling. This is further evidence by the temperature measured after 10 minutes of constant illumination at the maximal capacity: 55.81 $\pm$ 1.09 ºC (=junction temperature of 69.3 ºC, *n = 10*).

BOX 2: The different programs within the OptoArm software

Program 1: The testing menu. This menu is used to set-up your experiment. The menu allows the user to select the intensity of the LED by changing the analog scale: 0-255 (buttons up and down) and to turn the LED ON at that intensity. This menu is ideal for adjusting the working-distance and incidence angle to gain the appropriate intensity before starting an actual experiment. Importantly, as long as the Arduino is powered, the set intensity will be saved and the standard for the other menu-options (Figure 10D – I/II, Table 2).

Program 2: The single run menu. In this menu the user can select the time of the light-pulse (Figure 10D – III/IV). The buttons are time-sensitive: the longer one pushes, the steeper the steps. There is standard a 1 second waiting step before the pulse when the run is started. When the run is completed, the users get the opportunity to rerun the assay, without setting the parameters again (Figure 10E, Table 2).

Program 3: The series pulse menu. In this menu the user cannot only select the time for the light-pulse, but also the waiting time (between two light-pulses) and the number of cycle-repeats (Figure 10D – IV-VI). By going up and down in the menu, the different parameters can be adjusted (Table 2). There is again a 1 second waiting step before the first pulse when the run is started. When the run is completed, the users get the opportunity to rerun the assay, without setting the parameters again (Figure 10E).

Figures

Figure 1

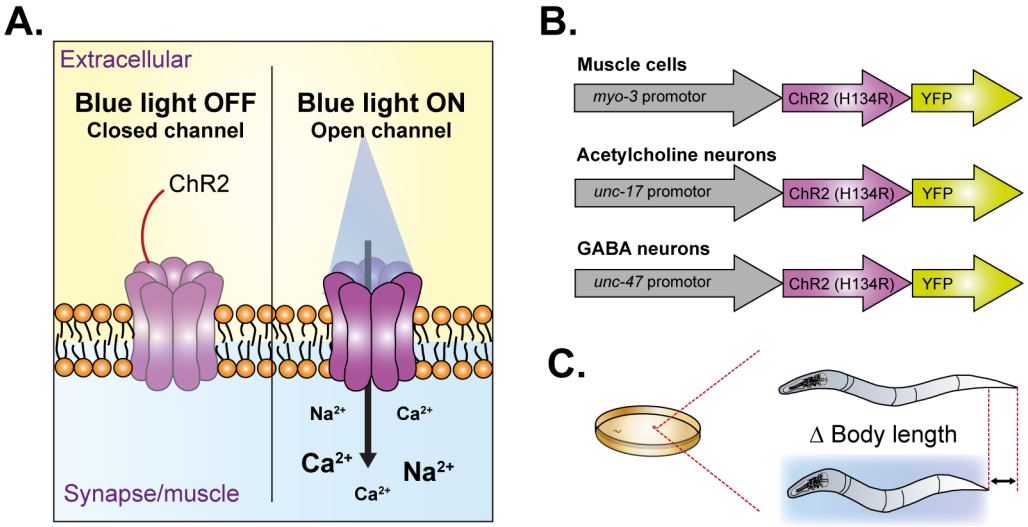

Figure 2

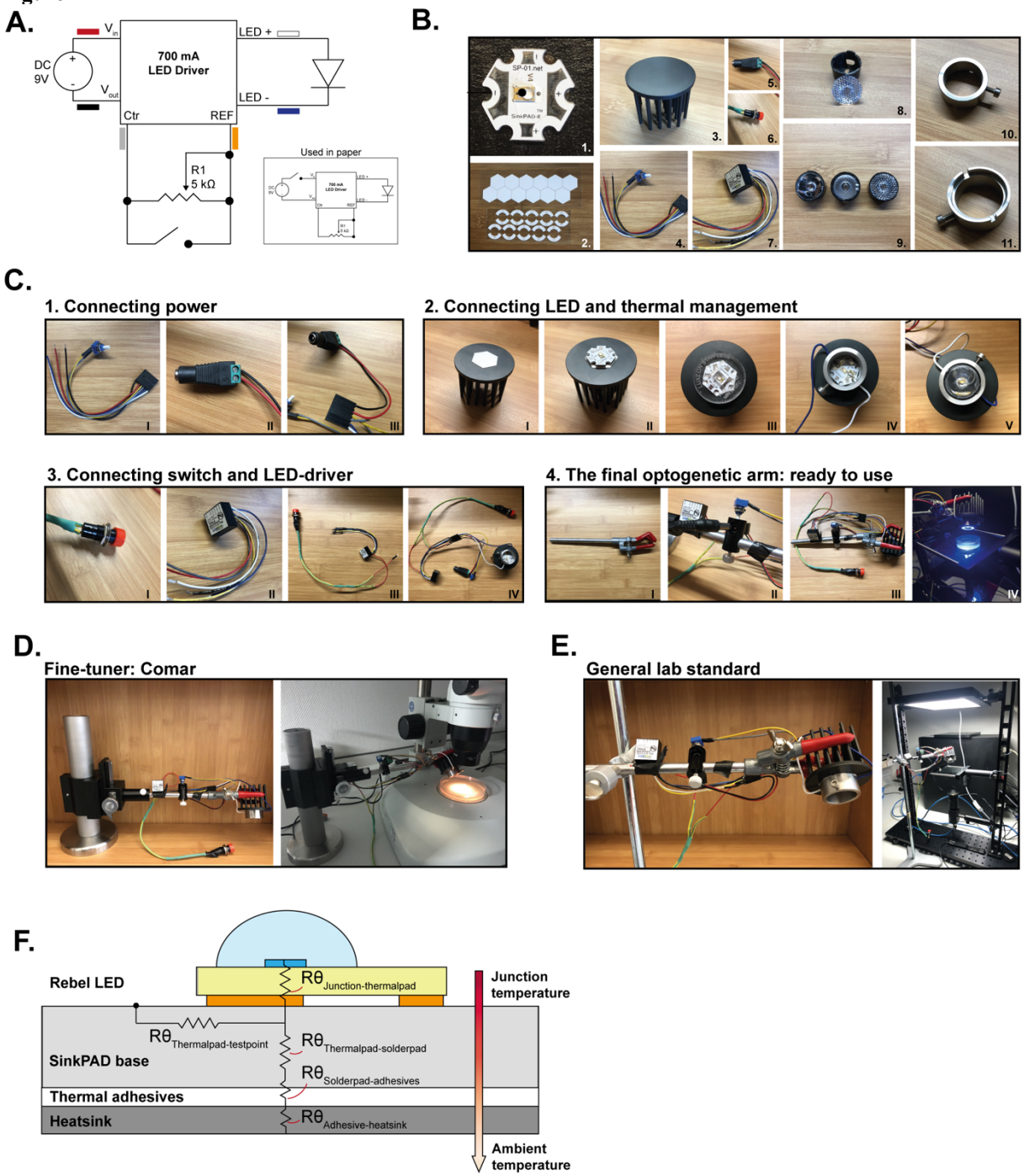
A.
DC
9V
V_{in}
V_{out}
700 mA
LED Driver
LED +
LED -
Ctr
REF
R1
5 kΩ
Used in paper
B.
C.
1. Connecting power
2. Connecting LED and thermal management
3. Connecting switch and LED-driver
4. The final optogenetic arm: ready to use
D.
Fine-tuner: Comar
E.
General lab standard
F.
Rebel LED
$R\theta_{Junction\text{-}thermalpad}$
Junction temperature
$R\theta_{Thermalpad\text{-}testpoint}$
$R\theta_{Thermalpad\text{-}solderpad}$
SinkPAD base
$R\theta_{Solderpad\text{-}adhesives}$
Thermal adhesives
Heatsink
$R\theta_{Adhesive\text{-}heatsink}$
Ambient temperature

Figure 3

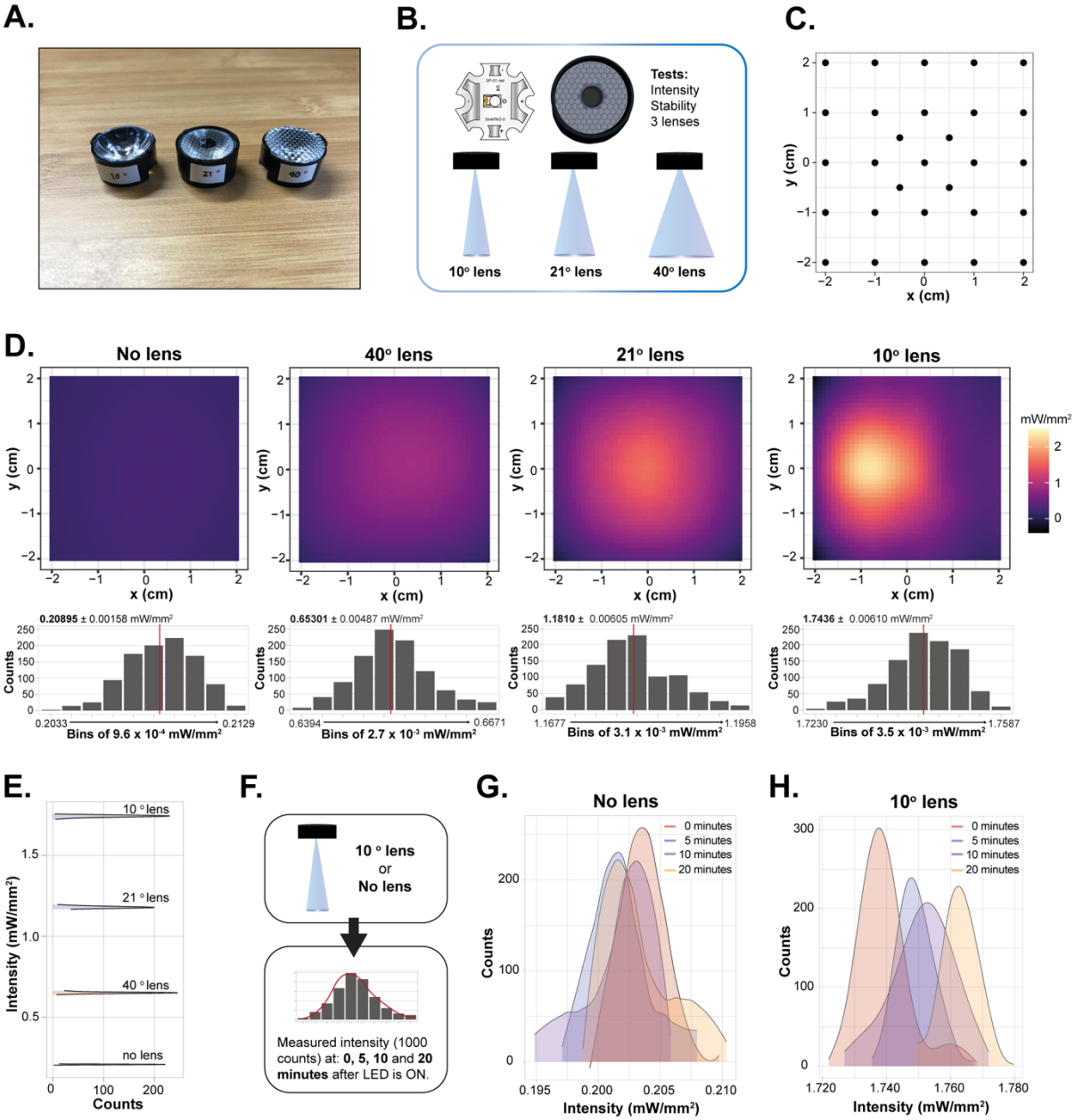
A.
B.
Tests:
Intensity
Stability
3 lenses
10° lens
21° lens
40° lens
C.
y (cm)
x (cm)
D.
No lens
40° lens
21° lens
10° lens
mW/mm²
0.20895 ± 0.00158 mW/mm²
Bins of 9.6 x 10⁻⁴ mW/mm²
0.65301 ± 0.00487 mW/mm²
Bins of 2.7 x 10⁻³ mW/mm²
1.1810 ± 0.00605 mW/mm²
Bins of 3.1 x 10⁻³ mW/mm²
1.7436 ± 0.00610 mW/mm²
Bins of 3.5 x 10⁻³ mW/mm²
Counts
E.
10 ° lens
21 ° lens
40 ° lens
no lens
Intensity (mW/mm²)
Counts
F.
10 ° lens
or
No lens
Measured intensity (1000 counts) at: 0, 5, 10 and 20 minutes after LED is ON.
G.
No lens
0 minutes
5 minutes
10 minutes
20 minutes
Counts
Intensity (mW/mm²)
H.
10° lens
0 minutes
5 minutes
10 minutes
20 minutes
Counts
Intensity (mW/mm²)

Figure 4

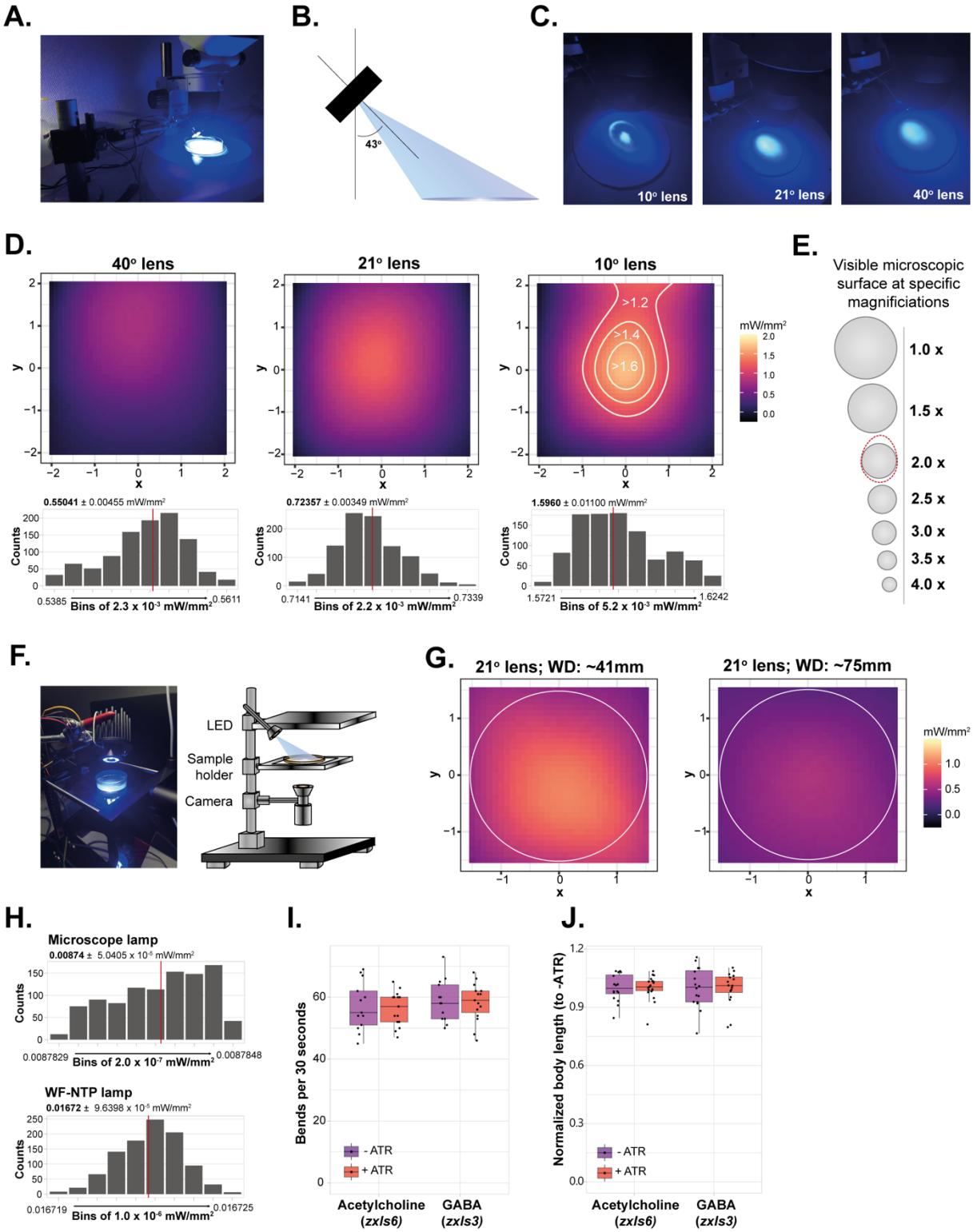
A.
B.
43°
C.
10° lens
21° lens
40° lens
D.
40° lens
21° lens
10° lens
>1.2
>1.4
>1.6
mW/mm²
x
y
Counts
0.55041 ± 0.00455 mW/mm²
Bins of 2.3 x 10⁻³ mW/mm²
0.72357 ± 0.00349 mW/mm²
Bins of 2.2 x 10⁻³ mW/mm²
1.5960 ± 0.01100 mW/mm²
Bins of 5.2 x 10⁻³ mW/mm²
E.
Visible microscopic surface at specific magnificiations
1.0 x
1.5 x
2.0 x
2.5 x
3.0 x
3.5 x
4.0 x
F.
LED
Sample holder
Camera
G.
21° lens; WD: ~41mm
21° lens; WD: ~75mm
mW/mm²
H.
Microscope lamp
0.00874 ± 5.0405 x 10⁻⁵ mW/mm²
Bins of 2.0 x 10⁻⁷ mW/mm²
WF-NTP lamp
0.01672 ± 9.6398 x 10⁻⁵ mW/mm²
Bins of 1.0 x 10⁻⁶ mW/mm²
I.
Bends per 30 seconds
- ATR
+ ATR
Acetylcholine (zxIs6)
GABA (zxIs3)
J.
Normalized body length (to -ATR)
- ATR
+ ATR
Acetylcholine (zxIs6)
GABA (zxIs3)

Figure 5

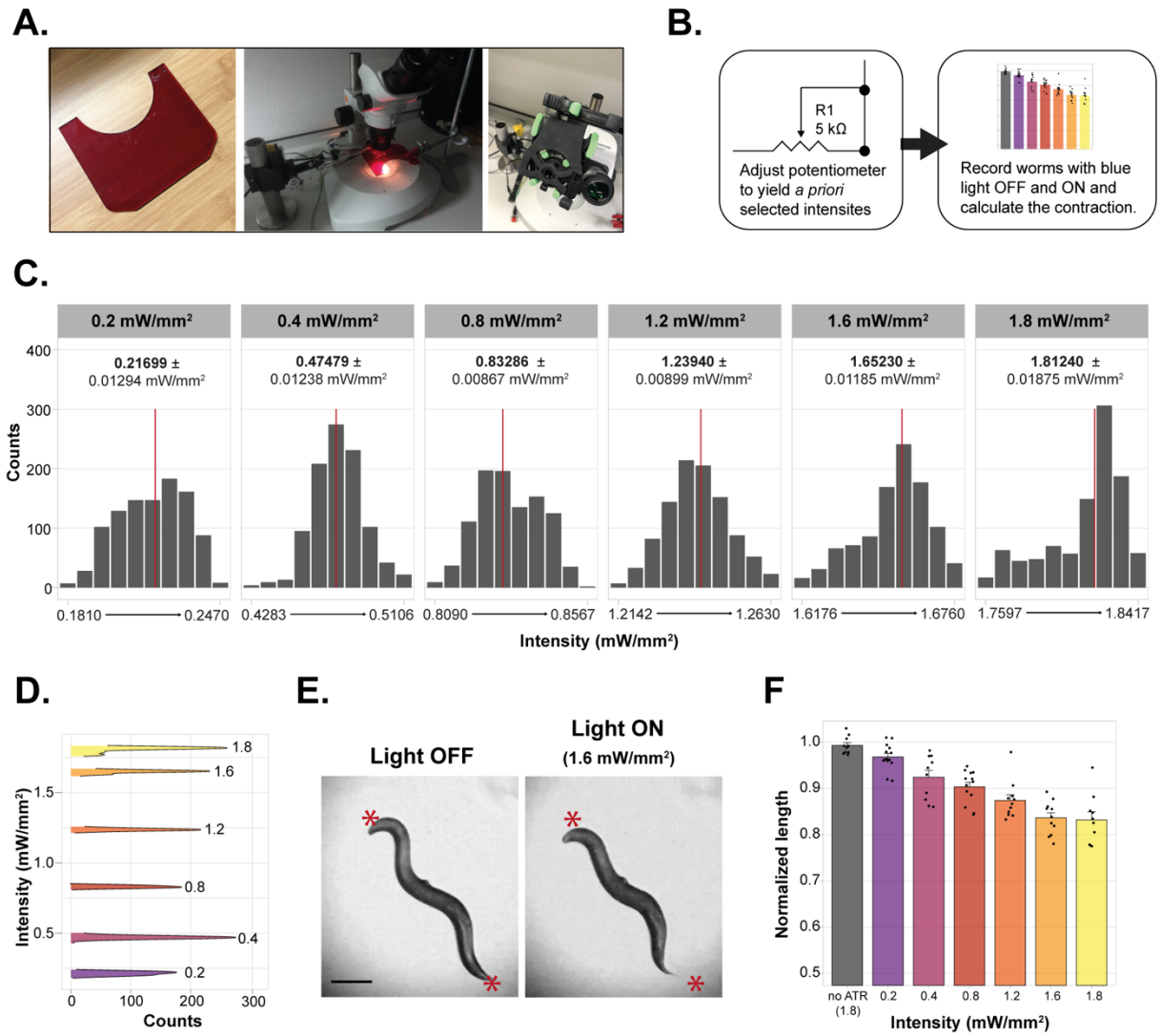
A.
B.
R1
5 kΩ
Adjust potentiometer to yield *a priori* selected intensites
Record worms with blue light OFF and ON and calculate the contraction.
C.
0.2 mW/mm²
0.4 mW/mm²
0.8 mW/mm²
1.2 mW/mm²
1.6 mW/mm²
1.8 mW/mm²
0.21699 ± 0.01294 mW/mm²
0.47479 ± 0.01238 mW/mm²
0.83286 ± 0.00867 mW/mm²
1.23940 ± 0.00899 mW/mm²
1.65230 ± 0.01185 mW/mm²
1.81240 ± 0.01875 mW/mm²
Counts
0.1810 → 0.2470
0.4283 → 0.5106
0.8090 → 0.8567
1.2142 → 1.2630
1.6176 → 1.6760
1.7597 → 1.8417
Intensity (mW/mm²)
D.
Intensity (mW/mm²)
Counts
E.
Light OFF
Light ON
(1.6 mW/mm²)
F
Normalized length
no ATR (1.8)
Intensity (mW/mm²)

Figure 6

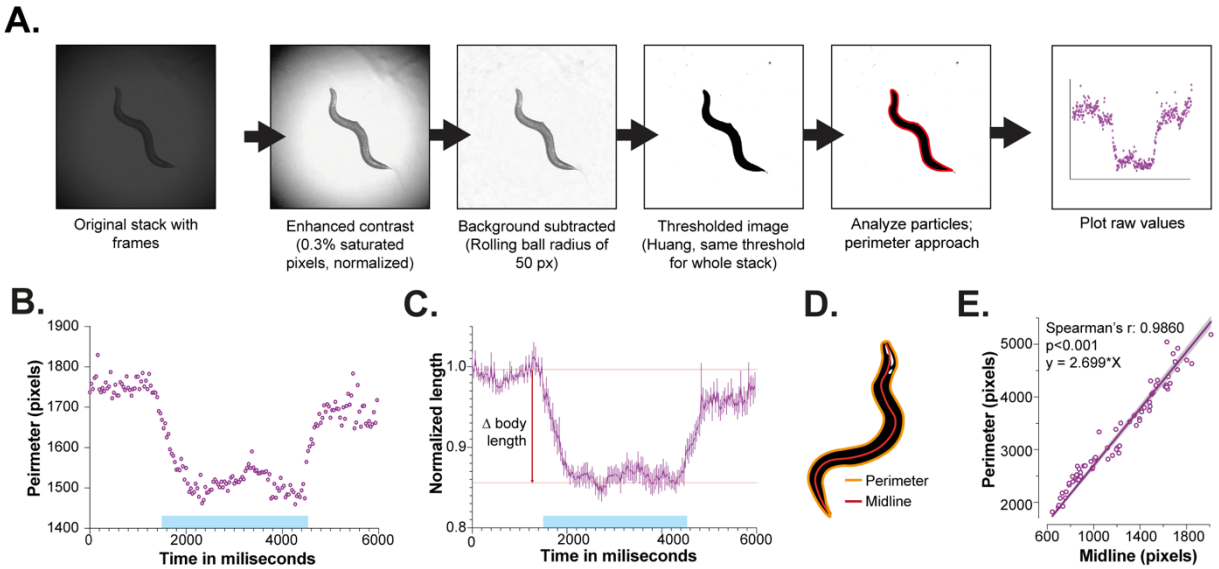
A.
Original stack with frames
Enhanced contrast (0.3% saturated pixels, normalized)
Background subtracted (Rolling ball radius of 50 px)
Thresholded image (Huang, same threshold for whole stack)
Analyze particles; perimeter approach
Plot raw values
B.
Peirmeter (pixels)
Time in miliseconds
C.
Normalized length
Δ body length
Time in miliseconds
D.
Perimeter
Midline
E.
Spearman's r: 0.9860
p<0.001
y = 2.699*X
Perimeter (pixels)
Midline (pixels)

Figure 7

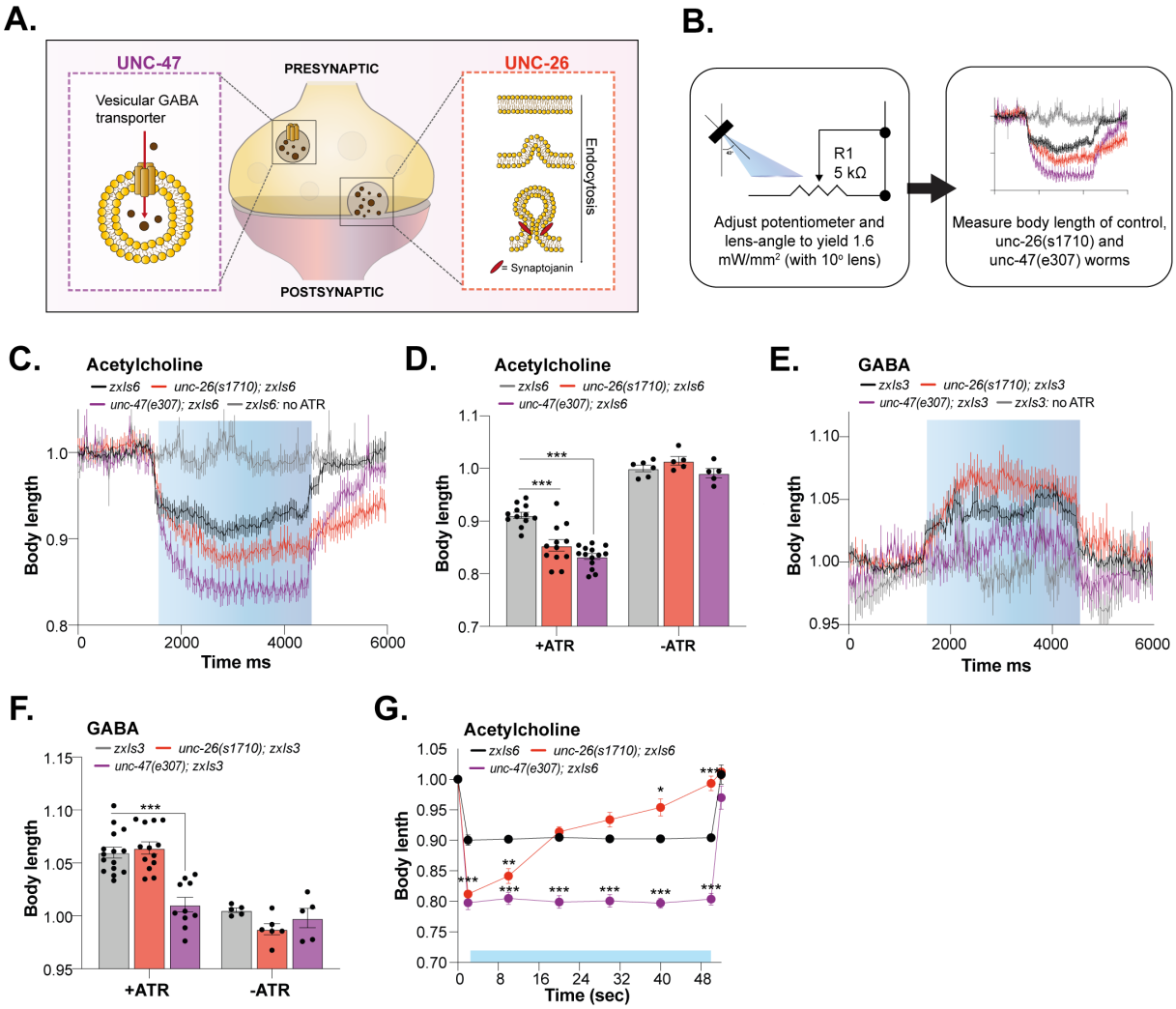
A.
UNC-47
Vesicular GABA transporter
PRESYNAPTIC
UNC-26
Endocytosis
= Synaptojanin
POSTSYNAPTIC
B.
R1
5 kΩ
Adjust potentiometer and lens-angle to yield 1.6 mW/mm² (with 10° lens)
Measure body length of control, unc-26(s1710) and unc-47(e307) worms
C.
Acetylcholine
zxls6
unc-26(s1710); zxls6
unc-47(e307); zxls6
zxls6: no ATR
Body length
Time ms
D.
Acetylcholine
zxls6
unc-26(s1710); zxls6
unc-47(e307); zxls6
Body length
+ATR
-ATR
E.
GABA
zxls3
unc-26(s1710); zxls3
unc-47(e307); zxls3
zxls3: no ATR
Body length
Time ms
F.
GABA
zxls3
unc-26(s1710); zxls3
unc-47(e307); zxls3
Body length
+ATR
-ATR
G.
Acetylcholine
zxls6
unc-26(s1710); zxls6
unc-47(e307); zxls6
Body lenth
Time (sec)

Figure 8

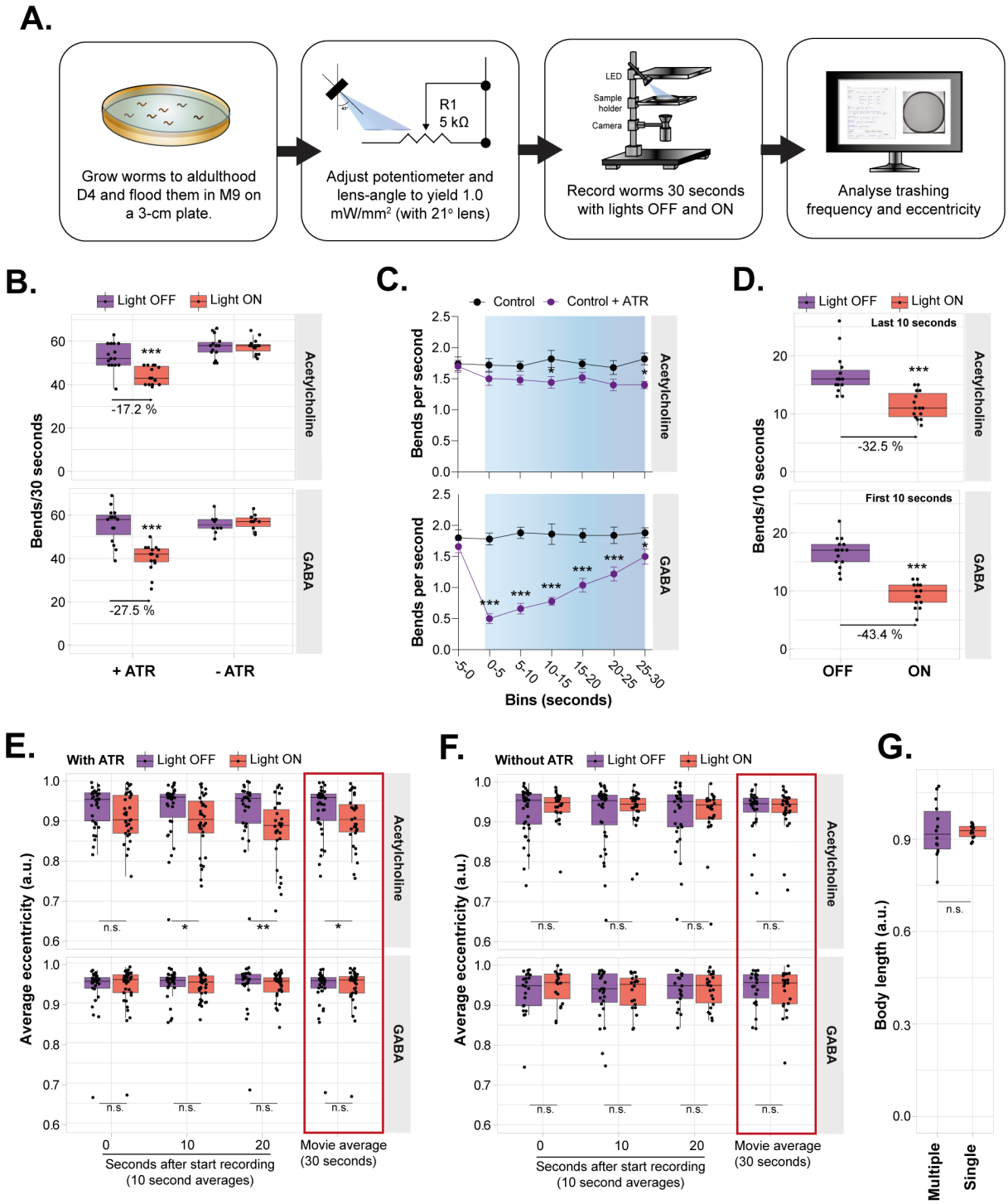
A.
Grow worms to aldulthood D4 and flood them in M9 on a 3-cm plate.
R1
5 kΩ
Adjust potentiometer and lens-angle to yield 1.0 mW/mm² (with 21° lens)
LED
Sample holder
Camera
Record worms 30 seconds with lights OFF and ON
Analyse trashing frequency and eccentricity
B.
Light OFF
Light ON
Bends/30 seconds
-17.2 %
-27.5 %
Acetylcholine
GABA
+ ATR
- ATR
C.
Control
Control + ATR
Bends per second
Bins (seconds)
D.
Last 10 seconds
First 10 seconds
Bends/10 seconds
-32.5 %
-43.4 %
OFF
ON
E.
With ATR
Average eccentricity (a.u.)
n.s.
Seconds after start recording (10 second averages)
Movie average (30 seconds)
F.
Without ATR
G.
Body length (a.u.)
Multiple
Single

Figure 9

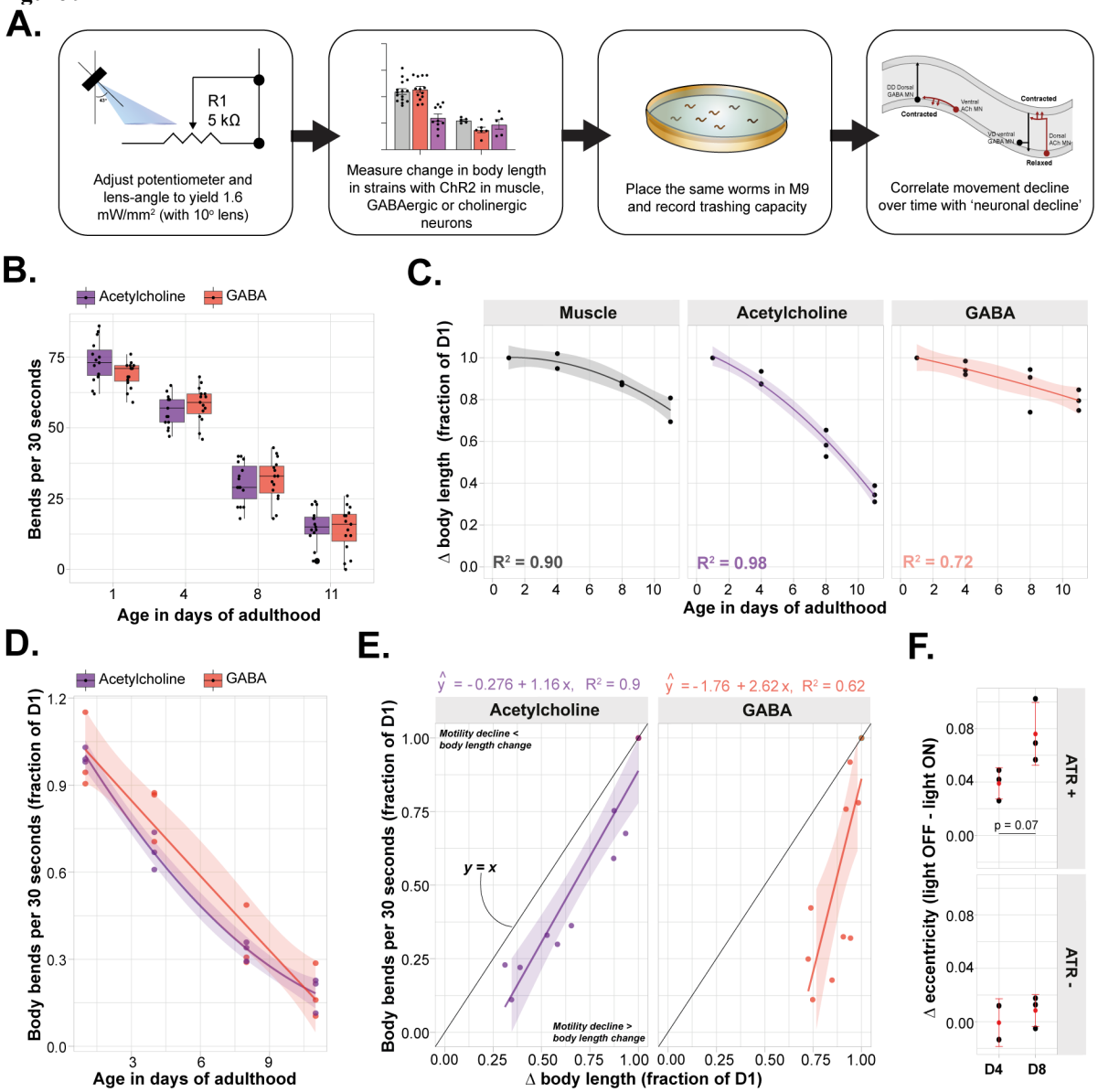
A.
R1
5 kΩ
Adjust potentiometer and lens-angle to yield 1.6 mW/mm² (with 10° lens)
Measure change in body length in strains with ChR2 in muscle, GABAergic or cholinergic neurons
Place the same worms in M9 and record trashing capacity
Contracted
Contracted
Relaxed
Correlate movement decline over time with 'neuronal decline'
B.
Acetylcholine
GABA
Bends per 30 seconds
Age in days of adulthood
C.
Muscle
Acetylcholine
GABA
Δ body length (fraction of D1)
R² = 0.90
R² = 0.98
R² = 0.72
Age in days of adulthood
D.
Acetylcholine
GABA
Body bends per 30 seconds (fraction of D1)
Age in days of adulthood
E.
ŷ = -0.276 + 1.16 x, R² = 0.9
ŷ = -1.76 + 2.62 x, R² = 0.62
Acetylcholine
GABA
Motility decline < body length change
y = x
Motility decline > body length change
Body bends per 30 seconds (fraction of D1)
Δ body length (fraction of D1)
F.
ATR +
ATR -
p = 0.07
Δ eccentricity (light OFF - light ON)
D4
D8

Figure 10

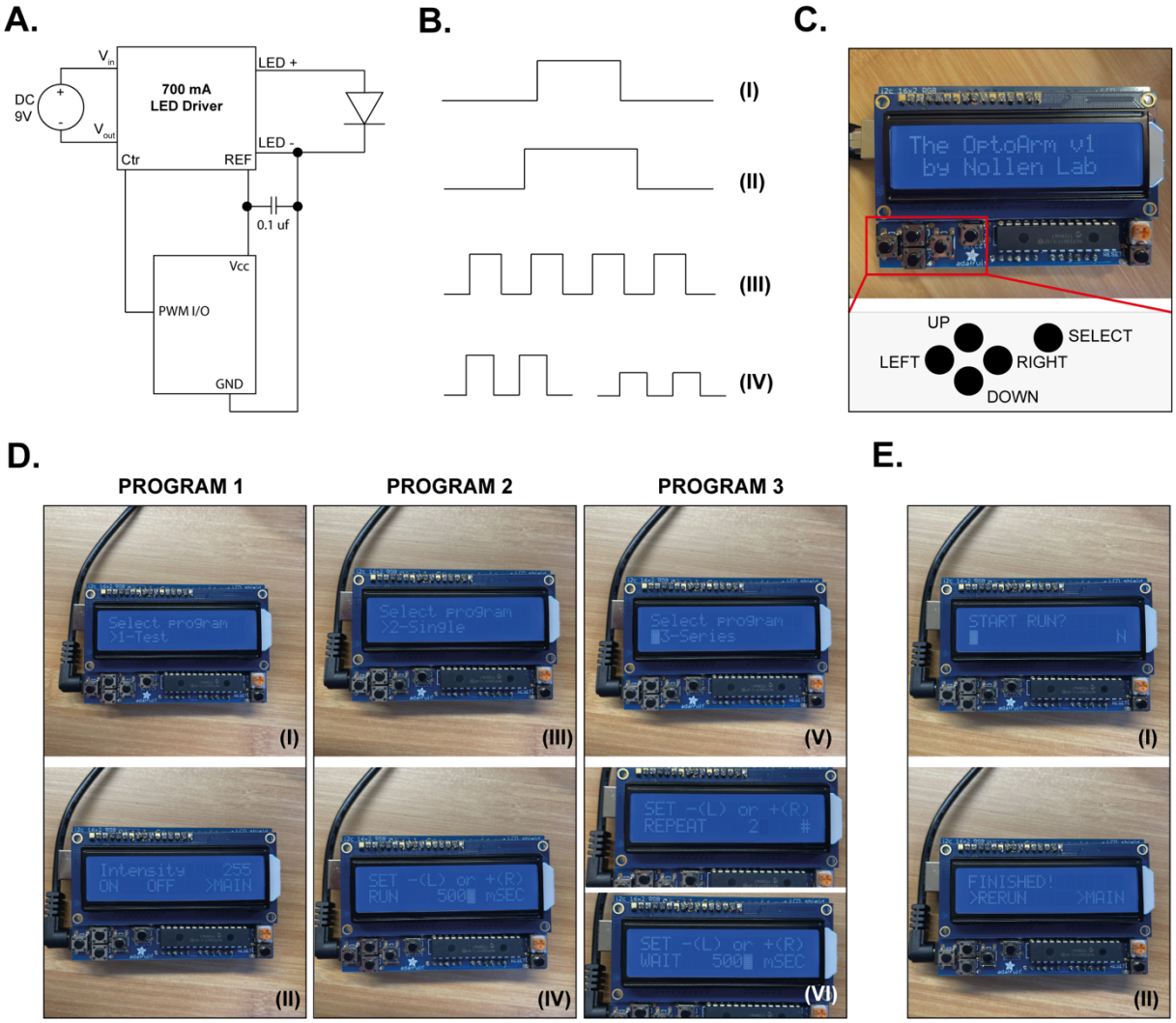
A.
DC
9V
Vin
Vout
700 mA
LED Driver
LED +
LED -
Ctr
REF
0.1 uf
Vcc
PWM I/O
GND
B.
(I)
(II)
(III)
(IV)
C.
The OptoArm v1
by Nollen Lab
UP
SELECT
LEFT
RIGHT
DOWN
D.
PROGRAM 1
PROGRAM 2
PROGRAM 3
Select program
>1-Test
(I)
Select program
>2-Single
(III)
Select program
3-Series
(V)
Intensity 255
ON OFF >MAIN
(II)
SET -(L) or +(R)
RUN 500 mSEC
(IV)
SET -(L) or +(R)
REPEAT 2 #
SET -(L) or +(R)
WAIT 500 mSEC
(VI)
E.
START RUN?
N
(I)
FINISHED!
>RERUN >MAIN
(II)